EXPLORING NANOSCALE CHARACTERIZATION OF LOW DIMENSIONAL ELECTRONIC MATERIALS

BY
ERIC SEABRON

THESIS
Submitted in partial fulfillment of the requirements
for the degree of Master of Science in Materials Science and Engineering
in the Graduate College of the
University of Illinois at Urbana-Champaign, 2015

Urbana, Illinois

Adviser:

Professor William Wilson

ABSTRACT

The advent of Atomic Force Microscopy (AFM) has allowed researchers to probe materials on the atomic scale with relative simplicity. For the study of nanoscale materials, structure is very important and often has a large impact on the materials intrinsic properties. The conventional form of Atomic Force Microscopy was developed to study material structure in the form of surface topography measurements. Since then there has been many advances which have taken advantage of the ability to detect small forces using an AFM tip along with surface topology.

A driving motivation in the scan probe microscopy field is the ability to spatially correlate properties of electronic materials such as charge density, conductivity, and doping distribution with nanoscale structure. Nanoscale characterization has become increasingly relevant as device features continue to shrink according to Moore's Law leading to the advent of next generation electronic materials such as semiconducting nanowires and Carbon nanotubes. The primary issue with measuring nanoscale materials properties is that the tip-sample coulomb forces and quantum effects that provide insight into the material's properties are very difficult to detect. A semiconducting Nanowire (NW) typically less than 500nm in diameter, is a quasi 1-dimensional structure with feature sizes approaching the diffraction limit of light rendering conventional optical spectroscopy ineffective; hence scan probe techniques are the most promising for characterization. Carbon Nanotubes, typically 1.0nm – 3.0nm in diameter, are 1-dimensional structures that are particularly difficult to characterize due to their infinitesimal sample volume. So far there has been very limited success electrically characterizing CNTs at the individual nanotube scale. Despite the challenges associated with nanomaterial characterization there have been successes at characterizing the electrical and chemical composition in parallel with

morphology using capacitance sensitive AFM techniques. In this study I will describe and present data from AFM techniques with the ability to characterize semiconducting nanowires and carbon nanotubes.

In chapter 1, there is a review of several variations of capacitive AFM used to measure electrical properties and chemical properties of nanomaterials, some of which require specific sample preparation making them incompatible with nanotube and nanowire characterization. Next, in chapter 2, is an introduction to Microwave Impedance Microscopy (MIM), a novel non-destructive scan probe technique we offer as a viable alternative for low dimensional electronic material characterization. The goal of Chapter 3 is to demonstrate the ability to measure the quantum capacitance of individual CNTs using MIM illustrating it's capability to measure nanoscale electrical phenomena. In chapter 4, MIM-AFM is used to provide insight into the structurally correlated doping dynamics of laterally grown GaAs nanowires. Finally, in chapter 5, a new scan probe technique called Near Field Infrared Microscopy (NFIR) is shown to be a complimentary characterization technique to MIM by probing the dopant distribution in GaAs nanowires. Many of the observations made using MIM-AFM and NFIR have never been seen before and could potentially have a high impact on nanowire device fabrication and characterization.

ACKNOWLEDGEMENTS

This project was made possible with the guidance of my mentor Professor William Wilson and my co-advisor Professor John Rogers. In addition I would like to thank my collaborators: Prof. Xiuling Li, Prof. Slava Rotkin, Scott MacLaren, Dr. Parsian Katal Mohsen, Dr. Xu Xie, Wonsik Choi. Lastly, I would like to acknowledge the Fredrick Seitz Materials Research Laboratory staff and my fellow colleagues for their collective help and support.

TABLE OF CONTENTS

CHAPTER 1: Overview of Scan Probe Based Microscopy Techniques……..……..1
1.1. Atomic Force Microscopy…….…....1
1.2. Kelvin Probe Force Microscopy …….……..…...2
1.3. Conductive Atomic Force Microscopy…….…....6
1.4. Scanning Capacitance Microscopy……. ……..…....8

CHAPTER 2: Microwave Impedance Microscopy for Electronic Property Characterization.....10
2.1. Introduction to Microwave Impedance Microscopy – Atomic Force Microscopy……..10
2.2. Instrument Overview and Calibration……..12
2.3. Image Acquisition……14

CHAPTER 3: Characterization of Individual Aligned Carbon Nanotubes using Microwave Impedance Microscopy ……...…….....21
3.1. Applications of Carbon Nanotubes……..21
3.2. Carbon Nanotube - Tip Model for Microwave Impedance Microscopy…….……25
3.3. Electronic Character Analysis of Carbon Nanotubes using Microwave Impedance Microscopy……...28

CHAPTER 4: Characterization of Doping Dynamics in GaAs Nanowires using Microwave Impedance Microscopy……....36
4.1. Applications of III-V Semiconducting Nanowires……...36
4.2. VLS Growth and In-situ Doping of Lateral GaAs Nanowires……...…….....40
4.3. Charge Density Profile Analysis using Microwave Impedance Microscopy ……..…45

CHAPTER 5: Near Field Infrared Spectroscopy/Microscopy Characterization of Doping Distribution in GaAs Nanowires……..……51
5.1. Introduction to Tip Enhanced Optical Spectroscopy/Microscopy…...…….....51
5.2. Theory of Near-Field Infrared Spectroscopy and Instrumentation…….….53
5.3. Doping Profile Observation using Near-Field Infrared Microscopy on GaAs Nanowires…….55

REFERENCES…….60

APPENDIX A: Microwave Impedance Microscopy – Atomic Force Microscopy Imaging Procedures……64

CHAPTER 1

OVERVIEW OF SCAN PROBE BASED MICROSCOPY TECHNIQUES

1.1 Atomic Force Microscopy

Atomic Force Microscopy is a technique that can measure atomic scale variations in the topography of a surface in ambient conditions. The fundamental mechanism of the technique is the use of a nanoscale, atomically sharp tip to trace out the contours of a surface. The tip is so close to the surface that it can detect the van der walls forces of attraction and repulsion; these forces can be mapped to see sub-nanometer variations in surface topography.

An AFM tip is fashioned out of a cantilever, which is a long arm that extends to the surface. Depending on the length and stiffness of the cantilever, the tip prefers to oscillate at a particular frequency on the order of ~1-100kHz. As the tip approaches the surface it begins to interact with the forces between the tip and surface which can change the frequency, phase, and amplitude of oscillation of the cantilever near the tip. By bouncing a laser off of the backside of the cantilever onto a photo-detector these changes can be correlated to the free oscillations of the cantilever via a lock-in amplifier.

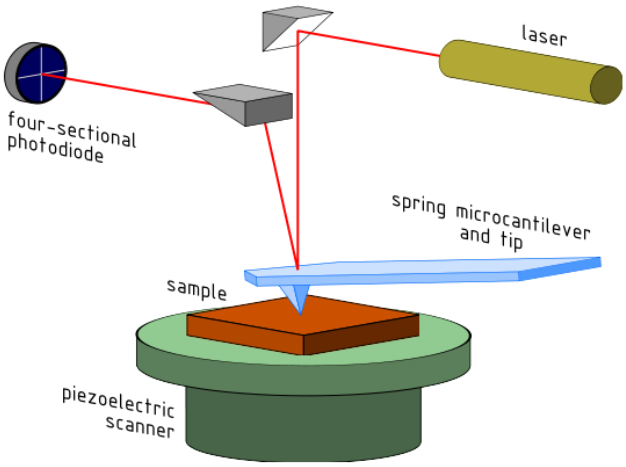

Figure 1.1: Simple model of an Atomic Force Microscopy configuration where the movement of the cantilever is recorded by the laser and laser diode.

The forces that govern the tip-sample interaction are not always dominated by van der walls forces, which are the primary forces for creating topographical images. Researchers have been able to create unique tips and tip-bias modulation schemes to enhance electromagnetic forces between the tip and surface. This allows for spatial mapping of other electronic materials properties in addition to topography.

1.2 Kelvin Probe Force Microscopy

Kelvin Probe –AFM (KPFM) is scan probe technique which using a conductive AFM tip and tip bias to drive electrostatic forces to map surface potential. The difficulty with Kelvin Probe and similar AFM techniques is that the correlation between the technique observables, frequency shift, amplitude, and phase, is often a nonlinear, complex function that involves a mixture of van der walls and coulomb forces [1,2]. However, these issues can be overcome by

using clever modulation tip bias schemes which can make vastly improve the sensitivity of the signal to only changes in surface potential. In general for KPFM both an AC and DC component is applied to the tip, $V_{tip} = V_{DC} + V_{AC}\sin(wt)$. The electrostatic forces that govern the tip-sample interaction is given by:

$$F = \frac{1}{2}(\Delta V)^2 \frac{\partial C(z)}{\partial z} \qquad (1.1)$$

Where $\Delta V = V_{tip} - V_{surf}$. The force felt by the tip can be reduced to the summation of the following three equations:

$$F_{DC} = \frac{1}{2}[(V_{DC} - V_{surf})^2 + \frac{{V_{AC}}^2}{2}]\frac{\partial C(z)}{\partial z} \qquad (1.2)$$

$$F_{1w} = \frac{1}{2}(V_{DC} - V_{surf})V_{AC}\frac{\partial C(z)}{\partial z}\sin(wt) \qquad (1.3)$$

$$F_{2w} = \frac{1}{4}V_{AC}\frac{\partial C(z)}{\partial z}\cos(2wt) \qquad (1.4)$$

The idea is that the amplitude of the F_{1w} signal is linearly correlated to the difference in the DC component of tip and the surface. By using a feedback loop to control Vdc to keep the F1W channel to zero, the relative magnitude of Vdc can be mapped as the surface potential [3].

There are many difficulties with using KPFM such as topology artifacts, tip separation dependence, and potential shielding from sample contaminants. To eliminate possible topology artifacts from van der walls forces KPFM typically operates in liftmode in which a two pass scan is implemented to minimize topology artifacts in the surface potential data [4] In liftmode, an initial pass obtains the AFM topology data and a second pass offsets the tip from the surface by a constant tip-surface distance, z, with the applied tip bias. Operating in liftmode also minimizes changes with tip shape and contamination, which is difficult to filter out. However, even with a

constant tip-surface distance the tip bias contribution to the surface potential can make it difficult to reproduce data and adds noise to the acquired signal. This is due to variations in z from non-linear van der walls forces, stray electrostatic forces from charging, and near-field tip effects when operating very close to the sample surface [1]. Lift-height variance can be mitigated by measuring FW1/FW2 to nullify the effect of $\frac{\partial C(z)}{\partial z}$ (refer to equation 1.1) and measuring the frequency shift [5]. The most critical issue with KPFM is its high sensitivity to contaminates and stray capacitances. These capacitances are averaged together in the surface potential data which can diminish the signal for the material understudy. Common sources of stray-capacitance noise are processing residue, oxide layers, trapped surface charges, and moisture [6,7,8].

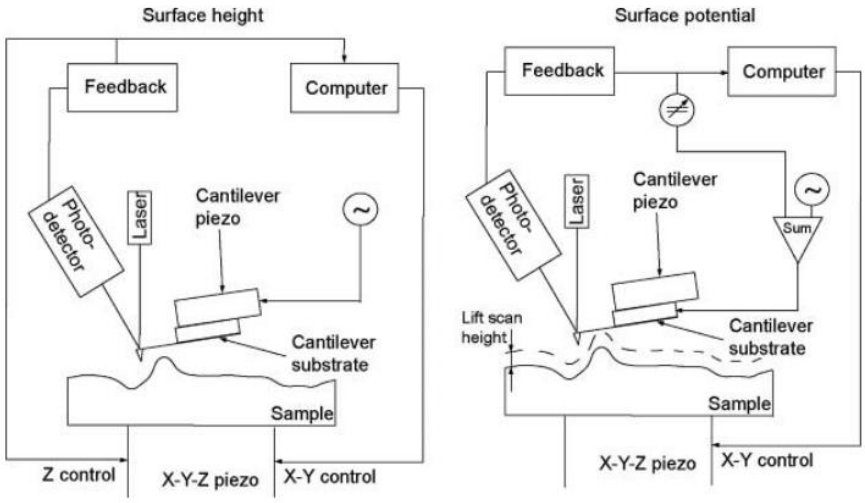

Figure 1.2: Shows the configuration differences between a basic AFM (left) and KPFM (right) setups [2].

KPFM has been useful in mapping changes surface potential on bulk samples with space charge regions, doping changes, and differing dielectric constants. However, using KPFM to measure nanoscale materials has been difficult, especially for ultra-high resolution charge density mapping. This is due to a diminished resolution and S/N ratio from the stray E-fields

which are large compared to the small signal change in surface potential from doping or defects [9]. Studies have successfully increased the signal to noise ratio of KPM on semiconducting nanowires and carbon nanotubes by adding metal contacts in order to inject charges from the source to the drain of the nanowire for improved surface potential contrast. This can be used to measure the mean free path which indirectly reveals the location of highly doped areas and defects since local scattering will be higher hence the equilibrium charge density will be lower [10].

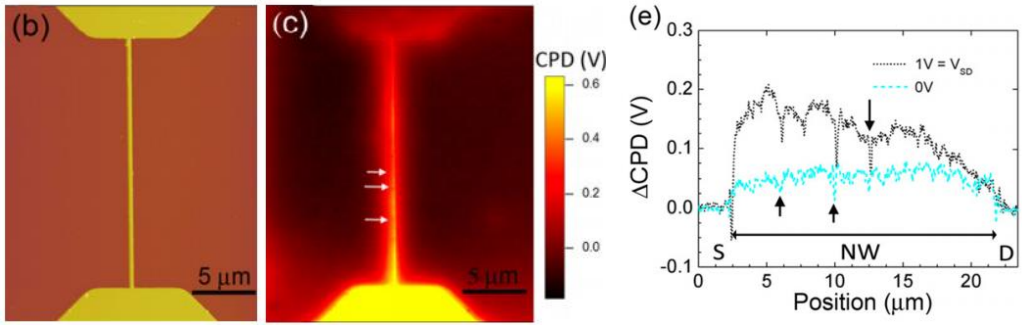

Figure 1.3: Shows an AFM image and KPFM image (top-left) of a p-doped Si Nanowire sample with ohmic contacts. On the bottom line cuts were taken of the KPM image to reveal regions of high electron scattering implying the presence of structural defects (top-right) [10].

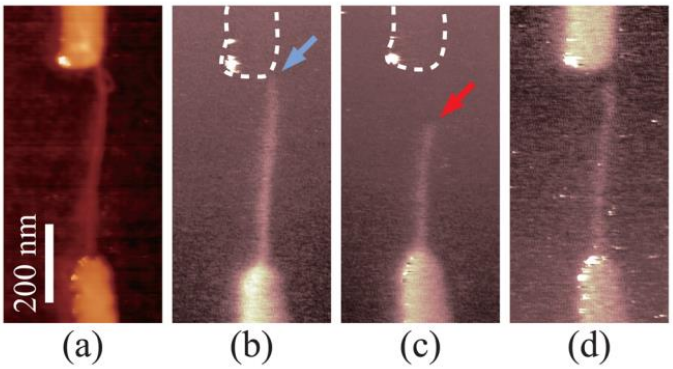

Figure 1.4: Shows an AFM image (a) and KPFM image (b-d) of a single Carbon Nanotube diode under different bias conditions. The arrow points to areas of differing contract, which is assumed to be causes by a scattering center [11].

Although KPFM-AFM has shown promise for electrical force mapping at a material's surface, it is evident that this technique is not ideal for nanomaterials. First, the only successful attempts at obtaining good images of the surface potential of NWs and CNTs (figure 1.3 and 1.4) have required the use of metal contacts which adds sample processing complexity which can be considered sample destructive. Second, the technique doesn't offer any pathway to spatially map the NWs local dopant density or their resulting electronic character.

1.3 Conductive Atomic Force Microscopy

Contact Mode AFM involves using the tip in direct contact with the surface in order to probe a wider range of material properties that require a direct contact such as hardness, elasticity, and conductivity. In this case the forces between the sample surface and the tip does not affect the oscillation of the cantilever, rather the force is directly measured through the tip-cantilever itself. One example of this is conductive AFM (C-AFM) which utilizes a metallically

coated tip and cantilever to measure the current though the tip itself. The spatial conductance can be directly measured by applying a bias to the tip creating a current through the material. This technique is limited because it relies a conductive path to a ground plane through the material [2]. This constrains its application to conductive materials and often requires metal contacts or backside ground plane making the technique less versatile. C-AFM data can be generated from either ohmic or tunneling current; this implies that many different material transport characteristics such as oxide thickness, defect density, or work function in addition to conductivity can create contrast. In addition, the flow of current in nanostructure semiconductors can cause hysteresis and changes in local material properties from surface charging adding more artifacts to the data. This makes this technique impractical for imaging specific electronic properties in highly susceptible electronic nanostructure.

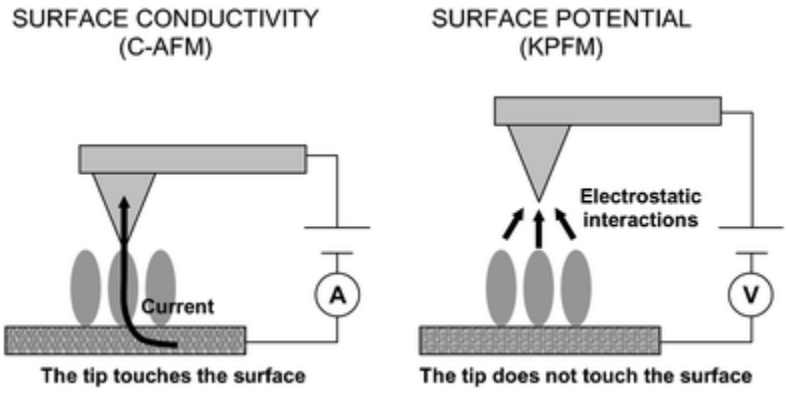

Figure 1.5: Shows the schematics of two different electrical AFM techniques, C-AFM (left) and KPFM (right) [12].

1.4 Scanning Capacitance Microscopy

Scanning Capacitance Microscopy is very similar to C-AFM in that it detects electronic properties in a material by operating in direct contact; however the capacitance across the sample is detected rather than the conductance. A capacitance sensor in the form of a LCR resonator is implemented in series with the tip and sample to detect spatial variations in capacitance [2]. To maximize the signal to noise an AC bias, typically much lower frequency than RF <10MHz, is applied to the tip to measure dC/dV phase and amplitude via a lock-in amplifier [13]. The signal is measured across the entire thickness of the sample from the tip to a ground plane on the backside of the sample. This way probing the sample solves the problem of needing a conduction path, the primary limitation of C-AFM. However, for SCM the signal observable, Delta C, response is proportional to AC signal amplitude; this means that for some materials the maximum sensitivity (~aF) requires a very high voltage AC signal [11]. The high voltage AC signal, which has a deep penetration depth, can modify the depletion width near interfaces and can shift the local Fermi energy level making intrinsic measurements difficult. Also, the deep penetration depth makes the effective tip-sample height (H) is on the order of the sample thickness causing the geometric capacitance to dominate the capacitance signal. The detected changes in geometric capacitance result from spatial changes in sample thickness, dielectric constant variations, and charge density. This makes SCM ideal for measuring local changes in doping concentration in quasi 2-Dimensional electronic materials [2]. However, for 1-dimensional materials its small volumetric cross section implies that its dielectric constant will only have a small influence on the measured average local dielectric constant of the subsequently large sample volume under the tip which diminishes contrast and sensitivity to the material understudy.

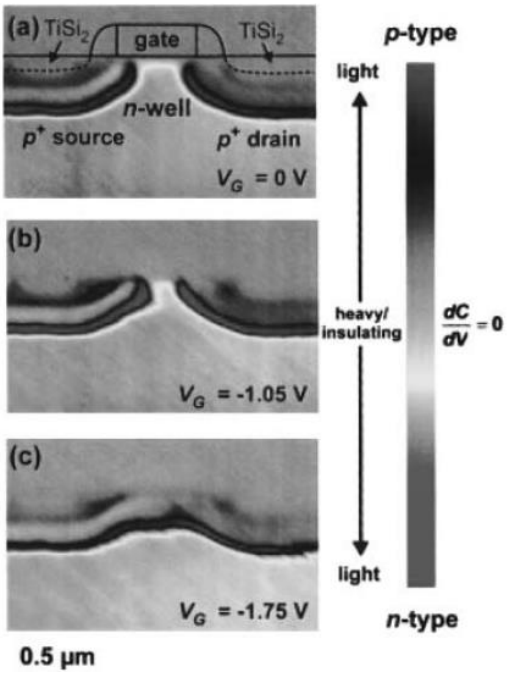

Figure 1.6: This is an SCM generated image of a Si based transistor cross-section. Notice that the contrast reveals the presence of a gate voltage controlled depletion region [2].

CHAPTER 2

MICROWAVE IMPEDANCE MICROSCOPY FOR ELECTRONIC PROPERTY CHARACTERIZATION

2.1 Introduction to Microwave Impedance Microscopy-Atomic Force Microscopy

It has been well known that the imaging of microwave reflectance could offer a unique window into the electronic response of advanced materials, directly probing their conductance, permittivity, and charge density [14,15,16]. A properly "tuned" microwave probe has minimal signal reflectance, which means that all the RF power is transmitted to the probe, but when coupled to an external materials system the impedance mismatch induced offers a sensitive probe of macroscopic electronic character. Near-field imaging allows microwave reflectivity measurements to be performed at the nanoscale by using a specialized AFM tip as a probe. Also, MIM benefits from being completely nondestructive and able to image in ambient conditions. Here, the microwave voltage reflectivity, Γ, is the detected measure of the microwave source tip to sample impedance mismatch, the quantity driven by the sample electronic characteristics. MIM-AFM spatially maps capacitance and resistance from the very small changes in reflectivity at the nanoscale (>20nm) and correlates the data to the topography data recorded by the AFM.

$$S11 \sim \Gamma = \Gamma_r + i\Gamma_i = \frac{Z_{sample} - Z_{tip}}{Z_{sample} + Z_{tip}}$$

$$\Gamma_i = \frac{2Z_{tip}X_{sample}}{\left(R_{sample} + Z_{tip}\right)^2 + X_{sample}^2}$$

$$\Gamma_r = \frac{R_{sample}^2 + X_{sample}^2 - Z_{tip}^2}{\left(R_{sample} + Z_{tip}\right)^2 + X_{sample}^2}$$

$$X_{sample} = \frac{1}{\omega C_{sample}}$$

It is worth emphasizing that MIM is a qualitative technique which measures small changes in reflection $\Delta\Gamma$, not the reflection coefficient itself. The tip impedance can be considered to be constant, whereas C_{sample} will be spatially dependent; in the limit where the sample capacitance is much smaller than the tip impedance, our observable $\Delta\Gamma(x,y)$ is linearly correlated to ΔC_{sample}.

$$\frac{\partial \Gamma_i}{\partial C_s} = \frac{4\omega Z_{tip}}{\left(C_s^{\,2}\omega^2\left(R_s + Z_{tip}\right)^2 + 1\right)^2} - \frac{2\omega Z_{tip}}{C_s^{\,2}\omega^2\left(R_s + Z_{tip}\right)^2 + 1}$$

$$\lim_{C_s \to 0} \frac{\partial \Gamma_i}{\partial C_s} = 2\omega Z_{tip} \equiv \alpha \Rightarrow S11 \sim \Gamma_i = \alpha C_s + \Gamma_{i0}$$

$$\Delta\Gamma_i(x, y) \sim \Delta C_{sample} \qquad \text{if} \qquad C_{sample} << \omega Z_{tip}$$

The RF signal has a shallow penetration depth which vastly improves the MIM's sensitivity to changes in capacitance present in the microwave near-field just below the tip apex. This is especially useful for mapping electronic character in nanoscale materials the electronic properties tend to lie at the surface. The sample volume under the tip is large enough to image through thin dielectric layers at relatively low RF power which enables it's use on semiconducting materials with a native oxide layer.

2.2 Instrument Overview and Calibration

The MIM-AFM system used for this research is composed of an Asylum MFP3D AFM, PrimeNano MIM electronics, a tip holder connected to a matching network via a coaxial cable, and a specialized MIM tip. The shielded cantilever probe is, "in essence" a high performance transmission line fabricated using a specialized co-axial AFM tip [17,18]. A matching network allows for the transmission of a low power RF signal, (~ -10dB at 3 GHz), down the apex of the tip to the sample. An unshielded contact pad makes a connection to the tip holder and subsequently the matching network and the rest of the MIM electronics. The signal reflected from the sample-tip interface is coupled into an RF Mixer. The electronics module captures the in-phase voltage reflection, Γ_r, and the 90 degrees out-phase component, Γ_i, of the signal.

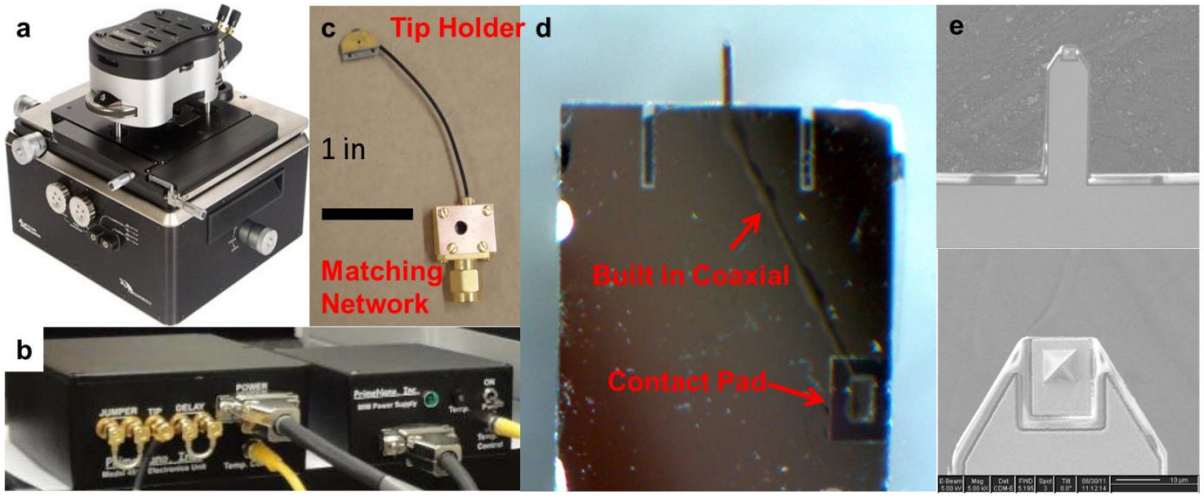

Figure 2.1: Image of MIM-AFM setup. (a) Picture of an MFP3D AFM. (b) MIM electronics (c) MIM tip holder with the matching network. (d) Probe showing the tip connected to a contact pad via a built-in coaxial. (e) SEM images of tip of a MIM-AFM probe.

The MIM returns the in-phase and out-phase components of the reflection in the form of voltage changes in the I and Q channel; the AFM controller spatially records the values along with the AFM topography data. Ideally, the reflection would be measured and recorded from the apex of the tip; however, there is a shift in the RF frame of reference due to differing path lengths of the incident and reflected signal in the electronics and the impedance mismatch between the matching network and the tip. This shift in the frame of reference makes the I and Q channel out of phase with the desired Real(S11) and Imag(S11) and must be corrected by doing a calibration.

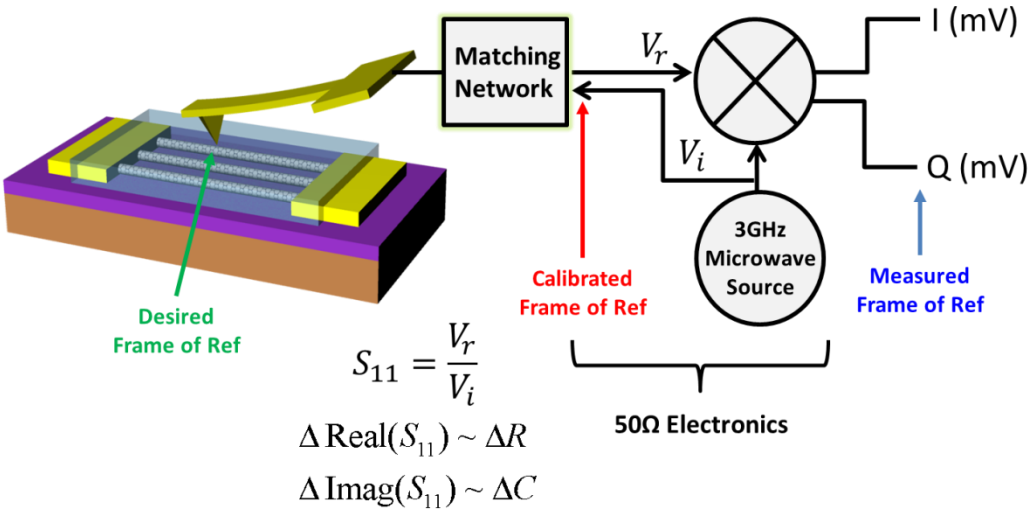

Figure 2.2: Simplified Diagram Showing the signal pathway in MIM.

The calibration is done by imaging a sample that is known to have areas with differences that are purely capacitive because there is a minimal difference in conductivity across the sample and a notable difference in charge density or dielectric constant. Typical calibration samples include alumina dots or doped regions of Silicon on a Silicon Oxide/Silicon substrate, but more

sophisticated calibration samples have been made to allow for a quantitative correlation of I and Q to Capacitance and Resistance. Since the contrast is only caused by capacitance changes, the mixer's phase offset can be tuned until all the signal is in either the I or Q channel implying that only one channel represents the capacitance and the other the resistance. After proper calibration both the resistive and capacitive channels are isolated and can be mapped spatially and displayed independently providing different information about the sample.

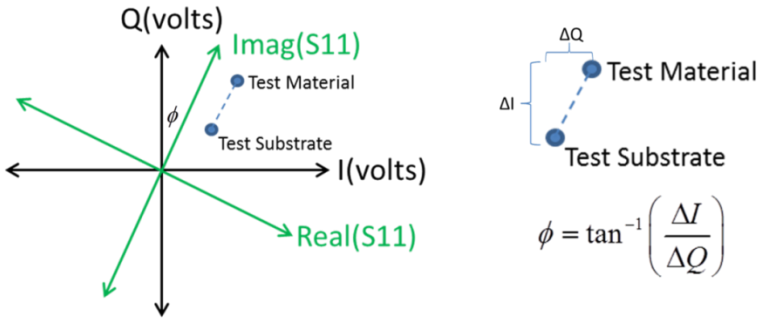

Figure 2.3: Diagram showing the basic concept behind using a calibration sample to correct for shifts in the frame of reference.

2.3 Image Acquisition

Image Acquisition in MIM-AFM is very similar to that of AFM. The procedure, which is outlined with more detail in appendix A, differs in the treatment of the tip; the goal is to minimize the wear of the tip as much as possible, and MIM calibration procedure. In general, one starts by load the MIM tip into the tip holder and secure the holder into the AFM; due to the small size and fragility of the MIM tips this was not a trivial task and required a lot of practice and finesse. Then the user preforms MIM calibration on calibration sample which will be explained in more detail in this section. Next, one loads the sample which is relatively flat,

feature greater than 500nm can be difficult to image with AFM. MIM is typically operated in contact mode to normalize the height dependence of the geometric capacitance. However, before acquiring MIM images the user should switch to tapping mode to find the specific area of interest. By using tapping mode to find the ideal area of interest, tip dulling and damage can be mitigated.

Once the tip and calibration sample has been loaded into the AFM one can begin the calibration procedure. Since every tip is slightly different and the matching network attached to the tip is not tunable, the only way to optimize the tip-matching network for maximum power transfer is to tune the operating frequency for the best free air reflection. While the tip is risen from the sample, we perform a frequency sweep from 2.7GHz to 3.3GHz to find a RF spectral dip indicating the ideal frequency for the least open circuit reflection, imply that most of the RF power is being transmitted to the tip apex. It is important that the dip is lower -20dB, if not then there may be problem with the MIM tip loading because not enough of the power is getting to the tip. Next we auto null the electronics which automatically adjust the internal tuning circuits to set the feedback voltages (I and Q) close to zero to keep the signal in the ±10V dynamic range. This offset should be recorded to ensure that signal drift isn't a problem during scanning. Signal drift can occur from changing local temperature, tip size, or the amount of RF power on the tip. Therefore, it may be necessary to auto null several during an image acquisition scanning session. It is worth mentioning that signal drift makes it increasingly difficult to obtain quantitative data from MIM.

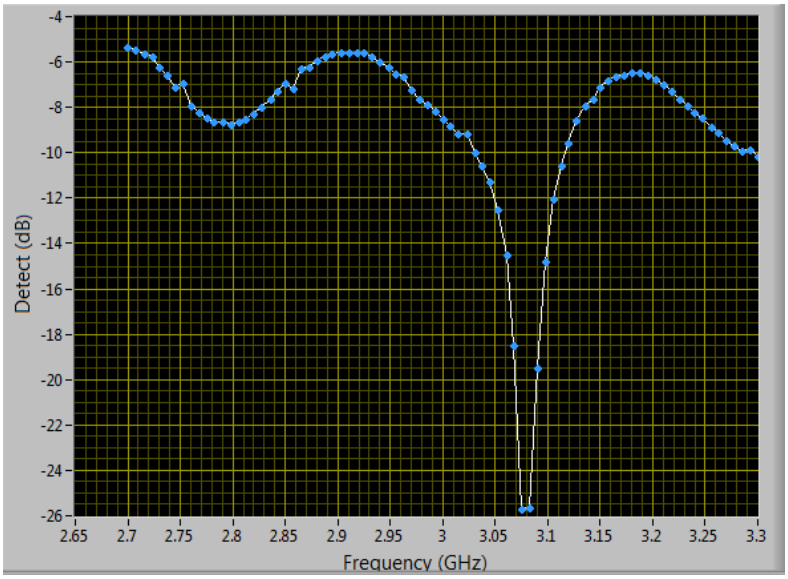

Figure 2.4: This is a typical RF resonance curve showing the exact frequency where the tip is best matched to the electronic implied by the sharp decline in signal rejection.

When setting the imaging parameters it is important to pick a scan speed and set point that will minimize wear on the tip to minimize artifacts. The set point indicates the amount of force that tip will contact the sample during the tip approach, the softer the tip approach then the less chance of damaging or dulling the tip when contacting the sample surface. The tip speed is also set fairly slow to ensure that the tip doesn't get damaged from tall (>500nm) features on the surface during the initial contact mode scan. When starting the scan it is important to move around the calibration sample until an Alumina dot in a clean region is found. Disabling a scan direction to ensure that the tip is scanning over the same area of the Alumina dot repeatedly is important to gather information about the signal to noise level.

Once scanning has started on the calibration sample it is time to perform the actual calibration step. We adjusted the mixer phase until all the signal is in either the I or Q channel.

One observation we made is that during calibration the signal in the resistive channel will never be completely nullified as seen in figure 2.5. The RF power going to the tip is preset to -10dB, increasing the "power set" on the component control panel will increase the sample volume which may also improve S/N. It may also cause hysteresis if set too high so we avoided going above -3dB whenever possible. During calibration check the S/N level, if it is too low then the tip may be too sharp or have a bad connection to the electronics. If the S/N <5 it typically meant that the tip was no good and therefore should not be used for imaging; this is likely caused by the tip coaxial wire damage or a bad connection between the tip and tip holder caused by dirt or poor tip design. We recorded the S/N ratio by taking a line cut of the Al2O3 dots, the higher the S/N the more contrast in the image. A Signal > ~±20mV is necessary for high quality images.

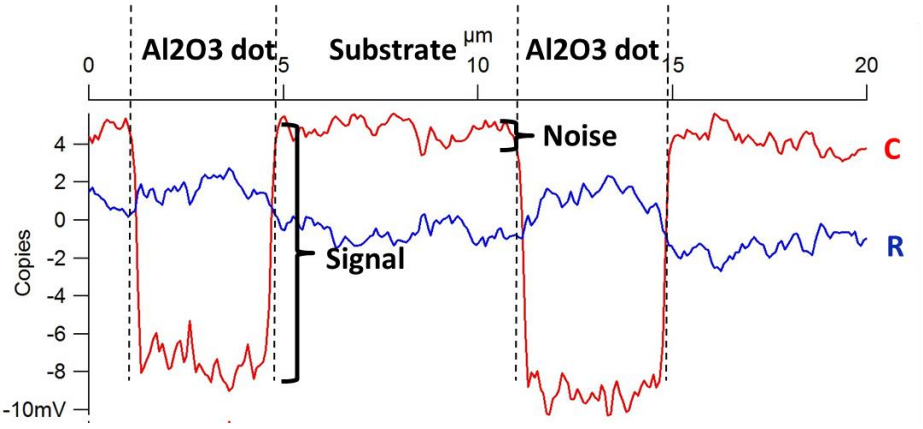

Figure 2.5: These are line scans of Alumina oxide dots on Si. Notice that after proper calibration there is very little signal in the resistive channel, R ~ Real(S11).

The MIM tip acts as a RF antenna, thus there is an inverse tradeoff between tip sharpness and S/N. In figure 2.6, simulations clearly show how signal is increased larger tip apexes [19]. For very sharp tips the signal to noise can be further enhanced, at the expense of spatial

resolution, by increasing the tip apex diameter which decreases the contribution of the geometric capacitance (C_g) in the capacitance signal and increases the sample size of the volume under the tip apex.

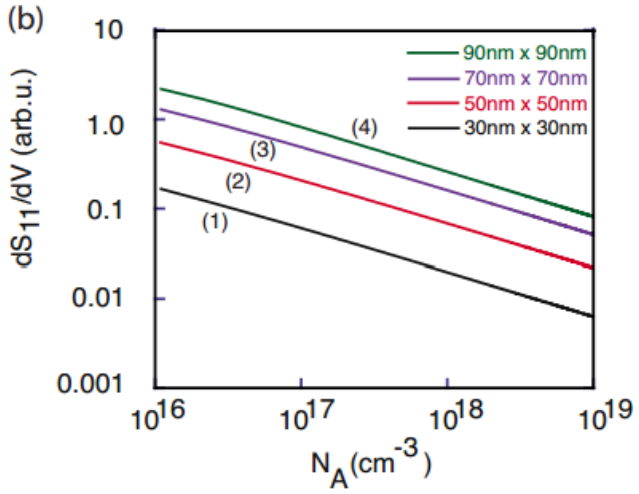

Figure 2.6: Simulation data showing the reflection dependence on tip size. Notice that the y-axis is plotted in log form implying that there is significantly more contrast (signal difference) available for moderately larger tips [23].

We were able to increase the S/N of our scan by increasing the set point which increases the force of the tip on the sample causing it to dull slowly. The tip can be dulled purposely according to the sample resolution tolerance and desired sensitivity/contrast of the scan. Tips will dull as the scan progresses according the relative hardness of the sample. We were able to increase the S/N by a factor of 2 or more after >150 scans. Once the desired S/N is obtained then we withdraw the tip and preform an auto null.

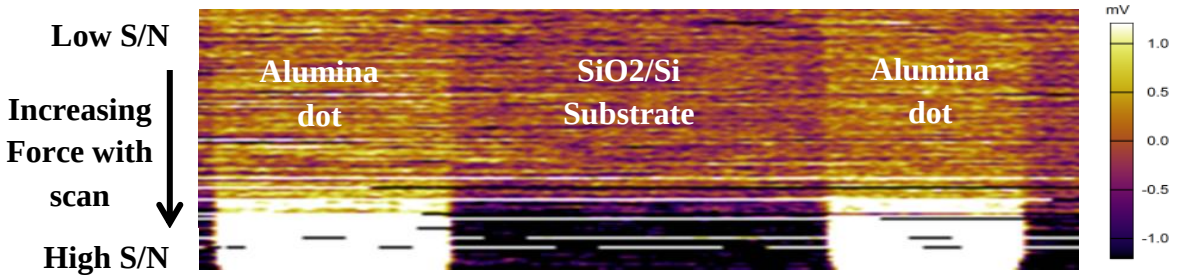

Figure 2.7: An example of how tip dulling can increase the S/N ratio. This is an image of repetitive line scans over the same region of the Alumina calibration sample with the set-point (tip force) slowly increasing in the direction of the white arrow.

Always record and save the Mixer phase and calibration images to figure out which pathway the C-signal is in and which direction is high Capacitance. The capacitance can be in either I or Q signal pathway and high capacitance can be negative or positive changes in voltage since it is possible for the mixer to be exactly 180 degrees out of phase. One way to tell if the MIM system is ready for high quality capacitive imaging is to create a 3D overlay plot of the calibration sample as seen in figure 2.8 to ensure that the color is fairly uniform on each feature and that the color contrast is sharp.

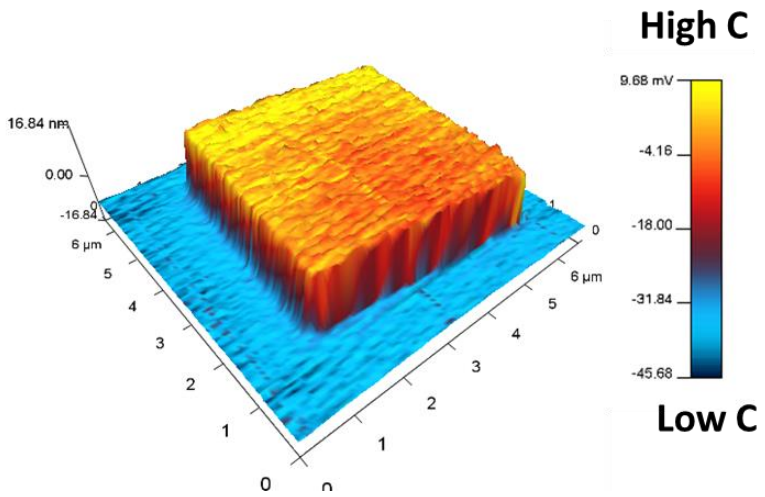

Figure 2.8: 3D capacitance/topography overlay of Alumina Dot used for Calibration.

CHAPTER 3

CHARACTERIZATION OF INDIVIDUAL ALIGNED CARBON NANOTUBES USING MICROWAVE IMPEDANCE MICROSCOPY

3.1 Applications of Carbon Nanotubes

Single-walled carbon nanotubes (SWNTs) are unique one-dimensional materials with structure driven electronic properties. Their intriguing transport behavior makes them an excellent candidate system for next generation device technologies including high performance, low power, RF field-effect transistors [20] and nanoscale logic devices [21]. Dense, horizontally aligned arrays of high purity semiconducting nanotubes [22,23,24,25,26,27] are the best development platform for these next generation device applications. This is due to the high charge carrier mobility, low threshold voltage, and potential to achieve ballistic transport all of which vastly improves switching dynamics.

Single Walled Carbon Nanotubes are essentially rolled up sheets of graphene, a carbon morphology that consists of a single atomic layer of carbon in a honeycomb lattice structure. Depending on the basis vectors which govern the way angle that the graphene sheet is rolled, the nanotubes can have varying electrical properties. Whenever, the difference between the basis vectors, also known as the chiral indices (m,n), are a multiple of three then the CNT forms a 0 energy bandgap making them metallic in electronic character. All other chiral indices form direct bandgap semiconducting carbon nanotubes, where the bandgap energy is inversely proportional to the diameter of the nanotube. The chiral indices also determine the diameter of the Carbon Nanotube, as seen in figure 29. This implies that as grown SWCNTs have will have a wide

dispersion of electrical properties which will pose problem in the material engineering of functional CNTFETs.

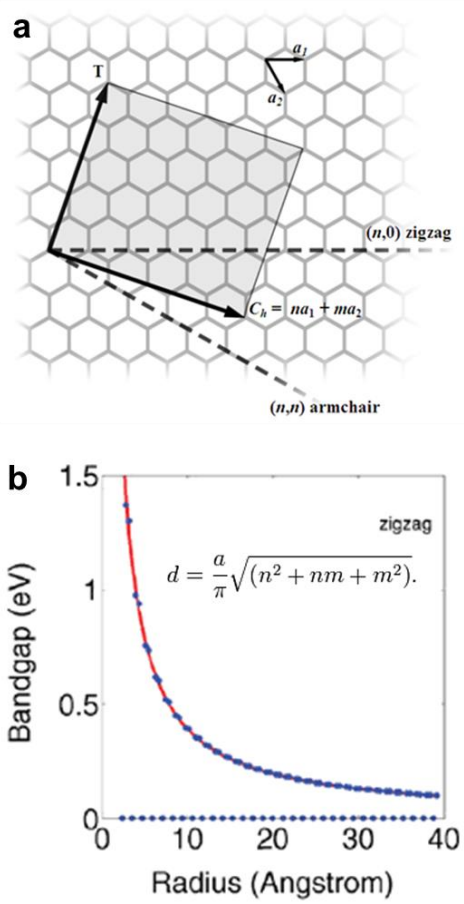

Figure 3.1: Visual representation of the how the lattice indices create different chiral structures in CNTs (top). Graph showing how lattice indices affect the diameter and bandgap energy of CNTs (bottom).

A typical Carbon Nanotube Field Effect Transistor geometry is shown in figure 3.2. Ballistic Transport is achieved when charge carriers can travel across the active region, between the source and drain electrodes, without a scattering event. This allows for the maximum group velocity of the charge carriers to be realized which vastly improves the transconductance and maximum cutoff frequency, which is greater than 1THz for CNTFETs. It is worth noting that

ballistic transport has not yet been achieved at room temperature, however, the potential to exploit ballistic transport through CNTs is a primary reason behind intense CNTFET research. In addition, the small bandgap energy compared to Silicon, ~0.3-0.8eV for CNTs and ~1.1eV for Silicon, implies that CNTFETs should have a notably lower power threshold for switching. The power consumption of devices is seen as a paramount issue in nanotechnology, which reiterates the potential impact that CNTs can have on the field.

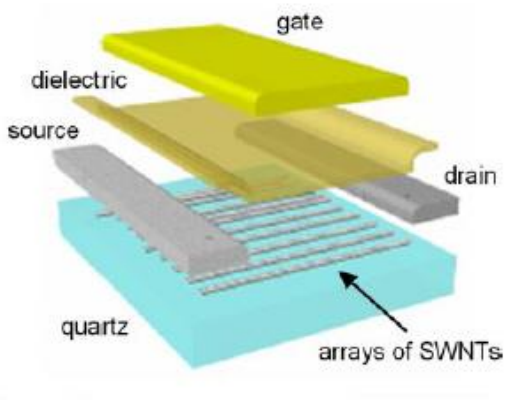

Figure 3.2: Simplified model of a top gated CNT Field Effect Transistor.

The difficulty of achieving high performance CNTFETs has been the inability to control the chirality dispersion described in section 4.0. Since ~33% of the CNTs grown are metallic, the device is often suffered from degraded transconductance. If even a few metallic nanotubes in a CNT array, the active region channel will be shorted leading to a high "OFF" state current. In addition, many larger diameter carbon nanotubes have smaller bandgap energies making them more susceptible to degenerate environmental doping creating semi-metallic nanotubes. These tubes, similar to metallic nanotubes make it more difficult to turn the active channel to its "OFF" state. This dispersion in nanotube electrical properties not only degrades the performance of

individual CNTFETs, but also limits scalability of creating such devices due to an increased variance in switching dynamics on a wafer scale.

Material Parameters	Ideal RF Applications [28]
Diameter	1.2-1.8nm
Purity	99.999% Semiconducting
Length	> Channel Length (~1um)
Alignment	All Parallel
Density	> 10 NT/um
Uniformity	Wafer Scale

Researchers have determined the ideal material parameters to create CNTFETs optimal for RF devices. Of the requirements, 100% purity, meaning all metallic CNTs in the array are removed, is one of the most important and difficult to achieve. Although there has been great promise in the creation of high purity arrays of CNTs, the research field still lacks the ability to characterize the CNT arrays with high precision and resolution. Currently, the leading method for obtaining purity values is to use Raman Spectroscopy characterization which lacks the resolution to characterize CNTs on the individual nanotube scale. Another common method of characterizing CNTs is to create large area array or single tube diode or FET devices and record there I-V response. This method can only provide indirect information about sample purity and can be considered sample destructive. Although purity values can be statistically interpolated from large area array data, the inability to characterize arrays on the individual nanotube scale has made it nearly impossible to optimize for purity and reproducibility.

3.2 Carbon Nanotube - Tip Model for Microwave Impedance Microscopy

The sample capacitance for a Carbon Nanotubes can be represented as a series capacitance summing the contribution from the static EM coupling of tip to the sample ie the geometric capacitance (C_g), and the contribution of the finite number of charges in the small volume directly below the tip ie quantum capacitance (C_q) [29,30,31]. The sample-tip interaction for any scan probe capacitance measurement can be modeled from the following equation:

$$C_{sample}^{-1} = C_{geometric}^{-1}(\varepsilon_{sample}, H) + C_{quantum}^{-1}(\rho)$$

$$C_g = \frac{\varepsilon_i}{2 \ln \frac{4H}{D}}$$

Where H = tip - sample distance, D = diameter of the tip apex, ε_{sample}= average local dielectric constant, and ρ = local charge density.

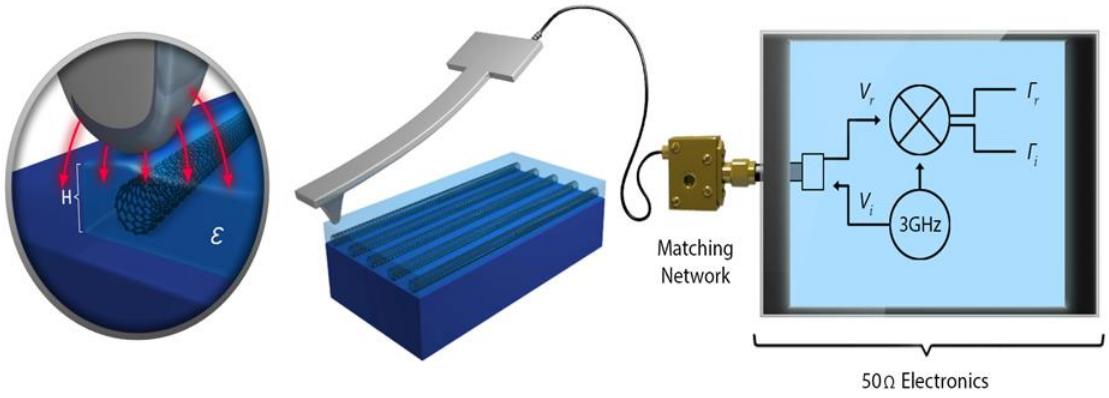

Figure 3.3: Simplified Schematic of the near-field microwave reflection geometry utilized.

If we explore applying this technique specifically to nanoscale electronic materials; the physics of the tip – sample interaction offers an intriguing experimental opportunity. Since the penetration depth of the RF near-field is so shallow we can assume that the static EM field responsible for the geometric capacitance coupling terminates at the sample surface. Therefore in contact mode imaging the effective tip-sample distance is virtually zero making the geometric capacitance >> quantum capacitance. For carbon nanotubes, quantum capacitance dominates if: the tip-sample distance (H) much less than the tip radius, and a thin layer (~3.5nm) of a high dielectric material ($\mathcal{E}$>>1) is present between the tip and nanotube sample. Under these conditions C_g becomes larger than the C_Q, maximizing contribution of the latter to the total capacitance detected. If we optimize the system to eliminate stray capacitance noise by properly impedance matching the tip and isolating the characterization setup, the MIM signal becomes a direct probe of the quantum capacitance C_Q of the nanotubes, with the imaginary component of the reflectivity linearly correlated[32]. The stray capacitance (noise) term C_{bg}, and C_g can be made insignificant to the signal by proper choice of the overlayer material.

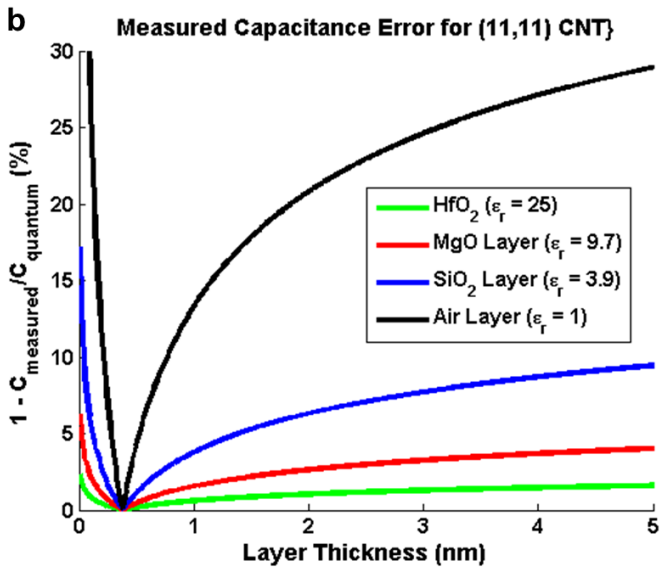

Figure 3.4: Graph showing the fractional contribution of the geometric capacitance to the total signal of a metallic (11,11) CNT as a function of dielectric layer thickness and dielectric constant.

C_Q is a function of the effective carrier density and the density of states, g(E). Given metallic tubes have a large number of free carriers, we expect a large C_Q or high capacitance for metallic species in an MIM image. Semiconducting tubes, (which, if intrinsic, should have a near zero free carrier density), should exhibit low capacitance. The equation for Cq for carbon nanotubes is:

$$C_Q = \frac{\sqrt{E^2 - \Delta^2}}{E} g(E)$$

Where 2Δ = Bandgap energy of the carbon nanotube. Assuming that $\Delta = 0$ for metallic carbon nanotubes, a simple model of the quantum capacitance of a semiconducting SWCNT relative to a metallic SWCNT is presented.

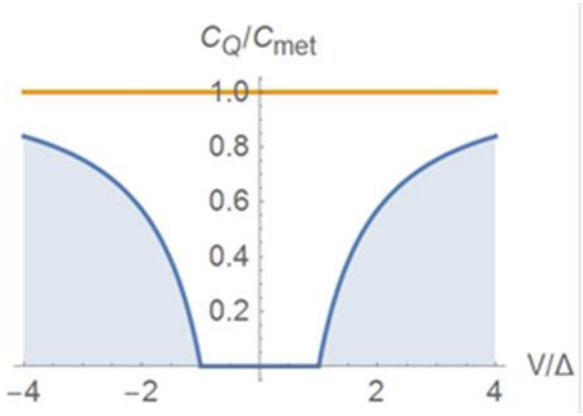

Figure 3.5: Simulation showing the quantum capacitance term for s-SWCNT, normalized to the metal Cq vs applied voltage in unit of Δ = Eg/2. Notice that the metallic NT has a much higher quantum capacitance than the semiconductor for a tip potential of 0V.

We have shown that given the scale of the relative signal contributions, if properly configured, the MIM observable is dominated by quantum behavior. This suggests MIM could be especially useful for electronic property mapping of individual Carbon Nanotubes.

3.3 Electronic Character Analysis of Carbon Nanotubes using Microwave Impedance Microscopy

For this study samples were grown using conventional Chemical Vapor Deposition using 0.5nm Fe catalyst lines deposited via Ebeam deposition on Quartz then thermally annealed for 1 hour. Growth is initiated by flowing a H_2 precursor gas through an ethanol bubbler into the growth chamber at 950C for 30 min. The step edges on 37^o cut quartz create surface adhesion forces which allows for highly aligned CNT growth. Densities of about 1-2 NTs per micron can

be achieved in our setup, although densities greater than 10 NTs per micron have been achieved using similar growth techniques.

Recently an innovative reflective near-field microwave imaging technology [33,34,35] was introduced; Microwave Impedance Microscopy (MIM) is a high resolution, scan-probe technique which offers the ability to spatially map material permittivity with a high sensitivity at 20-50nm resolution. Herein we report the application of scan-probe microwave reflectivity to the assessment of SWNT electronic properties. We use MIM to map the quantum capacitance of CVD grown, horizontally aligned SWNT arrays and show that metallic and semiconducting species can be easily and unambiguously identified.

Figure 3.6 shows MIM images of individual aligned nanotube arrays on quartz with an MgO overlayer (top) or a SiO_2 overlayer (bottom) respectively. We have additionally overlain the 3D AFM topology rendering with a color map revealing the spatially dependent capacitance detected. The expected signatures are clearly observed. In both images we detect a modest number of high capacitance nanotubes (of order 1/3 of the tubes in the field of view), consistent with the number of metallic nanotubes expected. Interestingly the contrast variance observed is strongly dependent on the properties of the overlayer. Note for the SiO_2 overlayer a large variance in signal is detected. This variation is driven by the RMS roughness of the sample's dielectric layer, (~0.2nm), and its direct impact on the contribution of C_g. Figure 3.2 importantly shows the impact of choice of the dielectric layer on the contrast observed for a nanotube array.

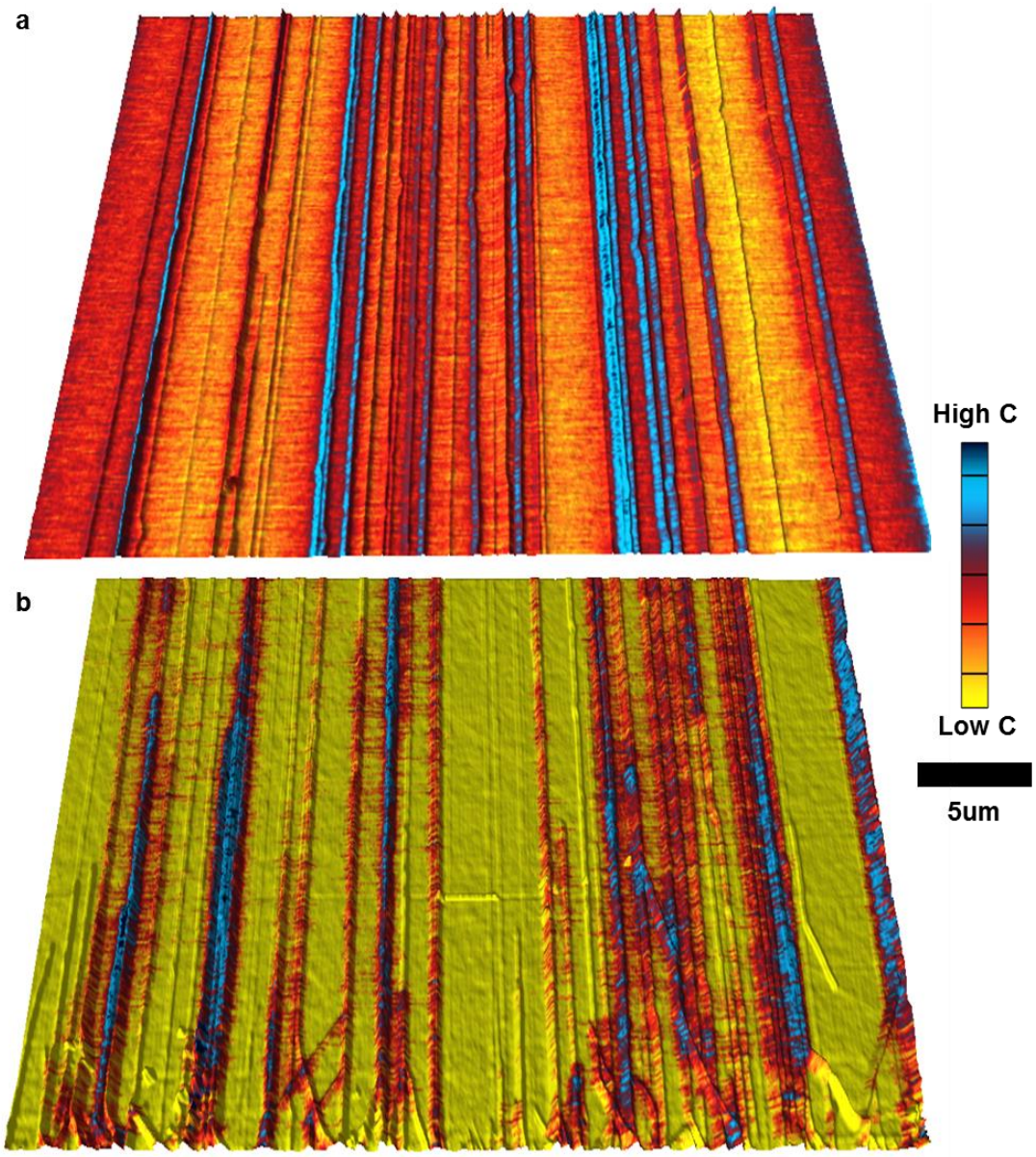

Figure 3.6: (a,b), MIM capacitance images overlaid on top of AFM 3D surface topology images of an array of CVD grown aligned SWNTs on quartz substrates. Each has a 3.5nm dielectric layer applied with (a) MgO used as the dielectric and (b) a SiO_2 layer utilized. The impact of the increased ε for MgO is very apparent resulting in improved contrast and uniformity.

The choice of SiO_2 with its modest Ɛ (3.9), results in a substantial contribution from C_g to the overall signal. Moreover a SiO_2 overlayer is permanent, limiting the potential of this technique for inspection. We subsequently switched to Magnesium Oxide as our overlayer choice. It offers two distinct values; first, its higher dielectric constant (9.7) substantially drives down the contribution from C_g causing dramatic increase in contrast uniformity. Although the MgO has comparable RMS roughness to SiO_2 (~0.2nm), the observed contrast is very uniform, consistent with minimizing the roughness contribution to C_g. Second and more importantly, the MgO deposited layer can be easily and completely removed with a simple mild acid rinse, making this technique versatile and completely non-destructive. After MgO removal, the nanotubes can be further processed into devices. The 3.5nm MgO overlayer was deposited by sputtering on at a rate of ~0.1A/s via Ebeam deposition. The samples then underwent a 15min thermal anneal on a hotplate at 400C to improve thin film uniformity. The samples were stored in a dry environment until used for MIM imaging. The removal of the dielectric thin film is done by submerging the samples in 20% aqueous HCL heated to 60C for 10min.

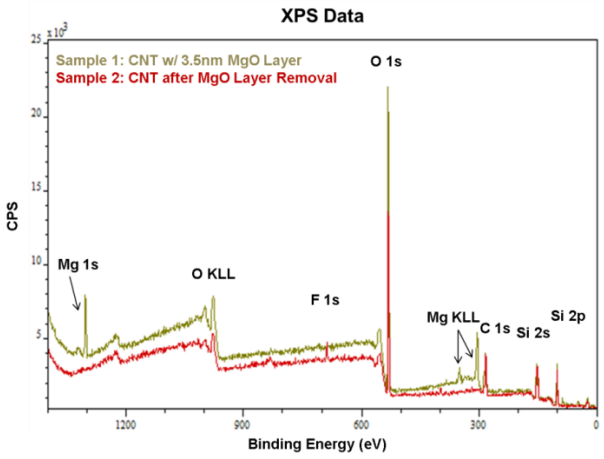

Figure 3.7: XPS analysis of a test structure before and after removal of a simple 3.5nm MgO dielectric layer.

The sensitivity and SNR of the capacitance channel are quite high, suggesting the potential of using MIM for electronic property inspection of Carbon Nanotubes. In this mode, the technique is non-destructive and can identify metallic and semi-metallic CNTs with high precision. One current limitation is spatial resolution, ~25-50nm (limited by currently available tips). This sets a limit of inspection to samples with CNT densities < ~20 NTs/um. Important is topography and capacitance image data are acquired simultaneously allowing for detailed nanoscale mapping of the correlations between nanotube diameter and electronic properties without the addition of contacts.

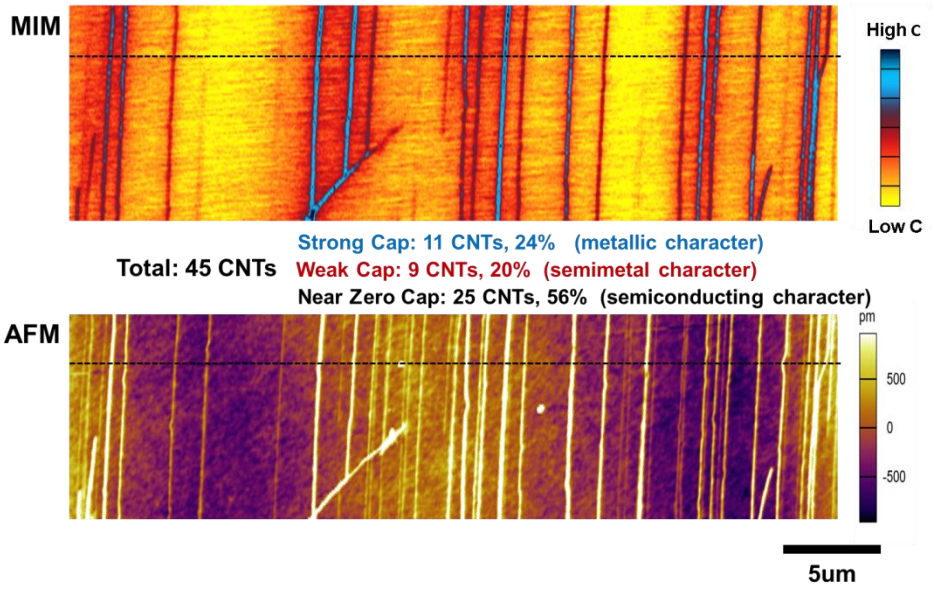

Figure 3.8: Direct comparison of MIM (top) and AFM (bottom) of a CNT array with 3.5nm MgO layer. The dotted line shows where the CNT counting statistics were gathered. NTs showing blue were counted as metallic, those showing red were considered semi-metallic, and those that don't show are assumed to be semiconducting.

MIM has considerable dynamic range in the capacitance channel making it very sensitive to overall nanotube electronic character. Carbon nanotubes are easily environmentally p-doped, the proximity of the electron density to the nanotube surface drives these processes. Observed property changes in nanotube devices when exposed to ambient oxygen [36,37] are excellent examples of this. This environmental doping is evident in the wide distribution of MIM capacitance that is seen experimentally.

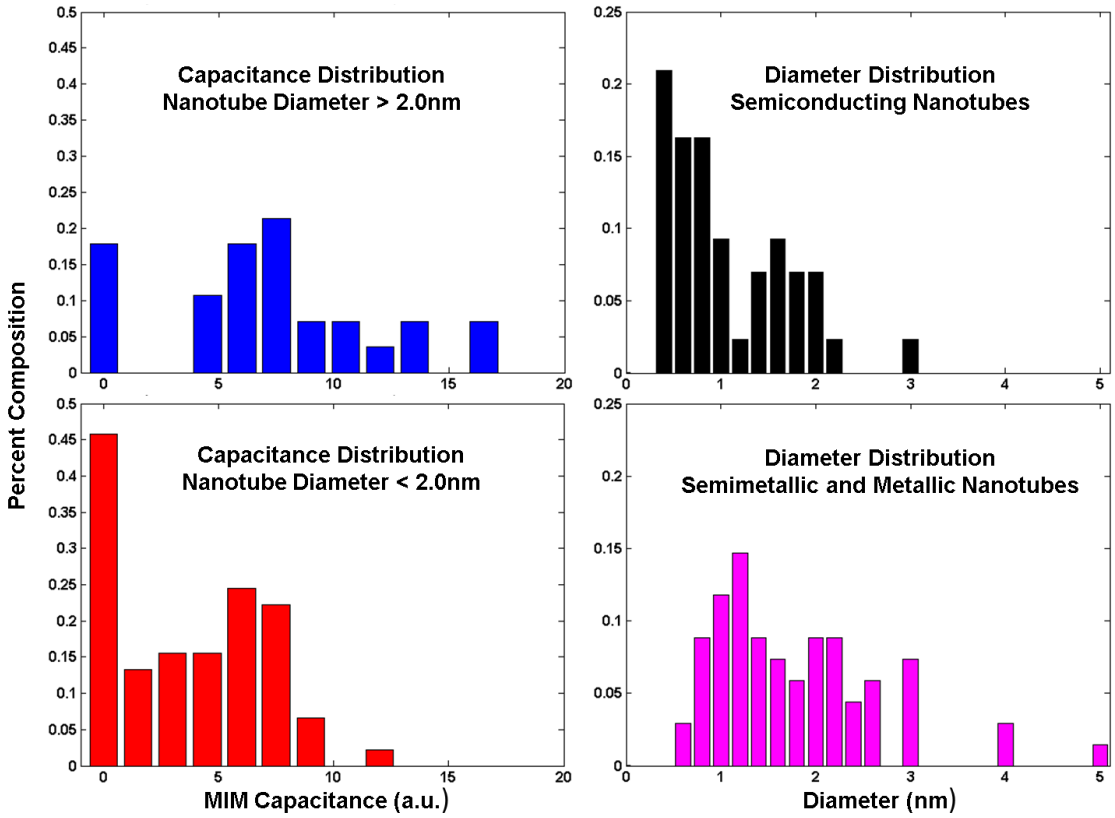

Figure 3.9: SWNT MIM capacitance and diameter distributions for the CNT arrays studied.

Notice that the non-intrinsic semiconducting nanotubes have larger diameter nanotubes. This is partly due to environmental doping of nanotubes, in which smaller bandgap, larger

diameter nanotubes are more susceptible to degenerate doping resulting in semimetallic behavior. However, we believe that another contribution to the increased number of large diameter, high capacitance nanotubes is bundling. Signatures of carbon nanotube bundling (figure 3.10) have been observed with MIM. Figure 3.10a shows formation of a m-SWNT/s-SWNT bundle. As expected the presence of a metallic nanotube in any bundle typically exhibits a high capacitance MIM signal suggesting, that any metal tube in a bundle shorts that bundle, "in essence" making it metallic. An s-SWNT/s-SWNT bundle is illustrated in 3.10b. In this instance the bundle maintains semiconductor character. Thus, is it simple to show that it is statistically more likely, 56%, that a two-nanotube bundle will show a metallic behavior than semiconducting behavior; whereas only ~33% of SWNTs show metallic behavior. This implies that the presence of bundles in a CNT array, which are sometimes difficult to identify, will lead to more nanotubes with metallic behavior than expected.

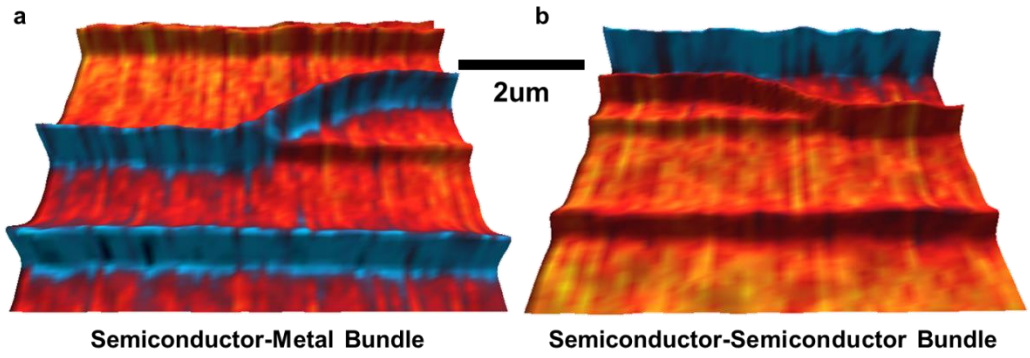

Figure 3.10: MIM images illustrating the observed signal for SWNT bundle formation. (a) s-SWNT/m-SWNT bundle; (b) s-SWNT/s-SWNT bundle.

Nanoscale microwave reflective imaging in this new geometry offers an extremely versatile “nondestructive” tool for nanotube characterization. We believe that this technique if used as an inspection strategy can have tremendous impact, allowing optimization of processing strategies including the development and optimization of scalable enriched growth, post-growth purification, and enabling detailed analysis of device-contact interactions.

CHAPTER 4

CHARACTERIZATION OF DOPING DYNAMICS IN GAAS NANOWIRES USING MICROWAVE IMPEDANCE MICROSCOPY

4.1: Applications of III-V Semiconducting Nanowires

III-V semiconducting nanowires (NW) have many properties that make them ideal for next generation RF transistor, VLSI, MEMS, and optoelectronic devices. III-V semiconductors have superior carrier mobility in comparison to Si which has been utilized to make higher performance FETs [38]. These types of transistors typically have very high cutoff frequencies, ~20GHz, due to their high saturation velocity [39]. Using III-V semiconductors in a nanowire structure has significant advantages including a finer control of the channel size and composition during growth. The ability to create small diameter nanowires increases the mechanical flexibility of the active region which allows for the creation of flexible electronics [40]. A major application of the III-V semiconducting nanowire technologies is RF electronics. There have been several demonstrations of vertically grown InAs nanowires in RF transistor geometries with cutoff frequencies above 100GHz, however since the metal contacts must be made as on top of one another the device suffers from challenging fabrication and a high drain-source parasitic capacitance [41]. Another primary drawback of III-V NW applications is the ability to control growth alignment and morphology [42]. The advantages gained by growing III-V semiconductors in a nanowire structure such as simpler processing and higher performance transistors is hindered by the need for complicated post-growth processing to get better alignment. The majority of the research on III-V NWs has focused on the growth of vertically

grown NWs, however in this chapter we will explore the growth and characterization of laterally grown NW which circumvents this issue to create better performance devices [43].

Creating smaller channel widths is a driving issue in VLSI electronics research. Nanowire architectures allow for the growth of nanoscale channel widths without complicated lithographic techniques, which makes Nanowires FETs an excellent candidate for next generation VLSI electronic applications. The primary appeal of III-V nanowires in the FET geometry is their ability to have higher power efficiency. To begin, the origin of the improved power efficiency of III-V nanowire devices from its superior charge mobility to conventionally used Silicon. This can be seen in figure 4.1, notice that every III-V semiconductor has a higher bulk electron mobility which is linearly proportional to conductivity [44]. This becomes increasingly important for VLSI electronics composed of nanoscale transistors because the mobility in the semiconducting channel decreases with smaller channel width determined by the relation $\mu \propto d^2$ [45]. This change in mobility is attributed to due to increased surface scattering which can be mitigated by using a capping layer on the nanowires to spatially isolate the active channel from the unfilled surface states.

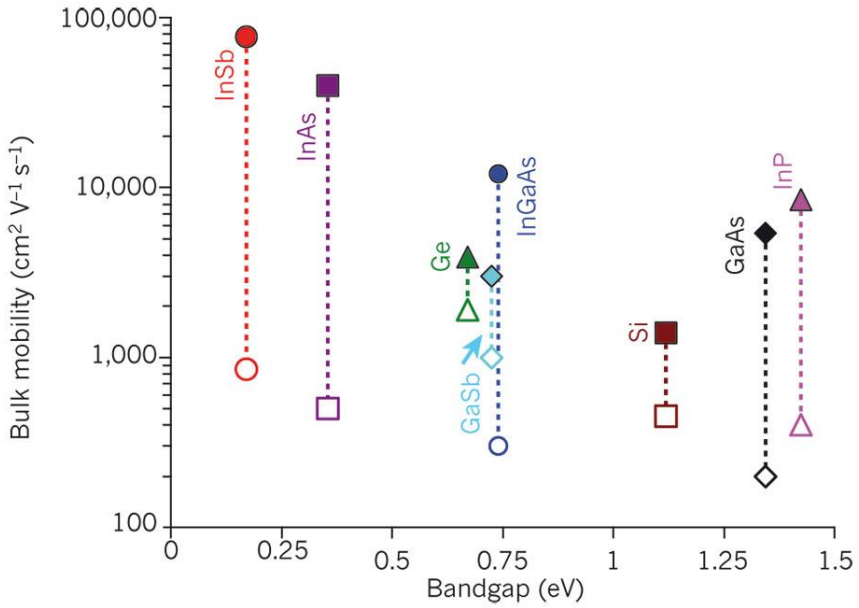

Figure 4.1: Graph showing the bandgap energy and charge mobility for electrons (color filled icon) and holes (unfilled icons) for various bulk semiconductors. Notice that the y-axis is in log form implying that small increases in mobility on this graph are actually quite significant [30].

Semiconducting nanowires offer an intriguing opportunity to create more desirable device geometries that can't be done with most bulk materials. Conventional high electron mobility FET designs rely on the formation of a 2-dimensional electron gas (2DEG) from the gate induced charge inversion layer. Charge inversion occurs as a result of band bending at the dielectric-semiconductor interface for gate voltages above the threshold (Vth). The current induced from gate voltages below the threshold voltage is considered loss power. With nanowires, a wraparound or tri-gate device geometry can be implemented which increase the overall area of the 2DEG in the inversion layer, which subsequently increases the current density capability of the active region [46]. Also, there is an opportunity to create very narrow nanowire transistors in a regime where quantum capacitance dominates, for substantial improvements in

maximum frequency and power consumption. In this regime the nanowire's electron gas is considered 1-dimensionally confined so long range charge screening effects do not occur making the depletion region width much more sensitive to the applied gate potential. This means that ideally there would be zero "OFF" current because of the large depletion region length and the formation of an electron gas via charge accumulation would happen very rapidly as the potential reaches the voltage threshold improving overall voltage swing of the device.

Another advantageous property of III-V nanowires is their bandgap can be easily engineered. The most apparent application of this property is the ability to tune the work function and bandgap of the drain and source ends of nanowire in order to make low resistance ohmic contacts via bandgap engineering for improved power efficiency performance. Researchers at IBM have proposed utilizing this feature to create tunneling Field Effect Transistors (TFETs) out of III-V semiconducting Nanowires. By tuning the work function and bandgap just right, the electrons from the source can tunnel into available valence band states in the channel when the device is "ON" [32]. However when the device is "OFF" the valence band energy of the channel is lower than that of the source electrons making tunneling impossible and a large energy ohmic barrier at the source minimizes leakage current [32]. Ideally, an III-V nanowire TFET would be very power efficient and would have a very high gain [32]. Researchers have also combined the tunability of the III-V semiconductor bandgap with the flexibility of Nanowires to create novel optoelectronic devices. Doped GaAs Nanowires were suspended by two metal contacts on a flexible substrate [47]. When uniaxial stress was applied to the NWs under an incident laser, the photoluminescence peak shifted as a function of strain from 1.25eV to 1.5eV. This change was attributed to strain induced conduction band splitting which changes the optical transition

energy. It is worth noting that the device configuration required the use of aligned lateral NW geometries.

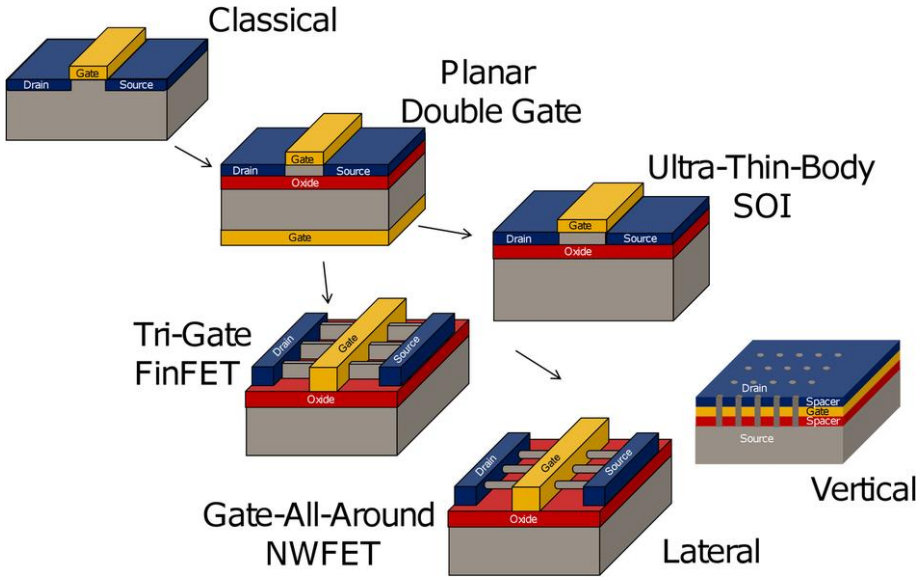

Figure 4.2: Simplified models of various FET geometries as they have progresses and will likely continue to progress with Moore's law. The two images on the bottom right represent future FETs with vertical and lateral NW architectures [48].

4.2: VLS Growth and In-situ Doping of Lateral GaAs Nanowires

The growth of the lateral III-V nanowires used for these studies (which will be explained in detail in this section) was performed by the Professor Xiuling Li group in ECE. III-V Nanowires have conventionally been grown III-V substrates using conventional lithographic techniques. More recently, the use of Metal Organic Chemical Vapor Deposition (MOCVD) has shown promise for creating these nanostructured materials. MOCVD is a high temperature (400-600C) growth process that utilizes a metal nanoparticle to catalyze nanowire growth via a Vapor-

Liquid-Solid mechanism. For GaAs nanowires the fundamental mechanism behind the growth is the adsorption of As vapor into the gold-Gallium alloy nanoparticle which acts as a growth catalyst. After the As concentration inside the alloyed catalyst, which is a liquid at peak growth temperatures, eventually hits supersaturation levels which causes single crystalline GaAs to precipitate out of the nanoparticle. The major advantage of using metal nanoparticles to grow nanowires is that the diameter of the nanowire is highly correlated to the size of the nanoparticle offering a pathway to creating quasi-1 dimensional structures without the need of advanced lithographic techniques [49].

The direction of growth prefers to follow a particular crystal orientation of the substrate to minimize the Gibb's free energy at the nanowire-substrate interface [49]. It been shown that the preferred growth orientation is highly dependent on the substrate crystal orientation at the surface and the growth temperature. GaAs NWs grown on (111) GaAs substrates prefer to grow out of plane creating vertical free standing NW structures (figure 4.3) [50]. However, vertically grown structures suffer from the formation of twin facets and stacking faults which limit the charge mobility in the axial direction of the NW. Also, vertically grown NWs must be etched away from the substrate and laid flat onto another substrate to make them compatible with conventional microelectronic processes which increases the processing complexity. For our samples (100) GaAs substrates are used for MOCVD growth at a temperature of 465C to promote planar growth. Since the planar grown GaAs nanowires prefer a particular growth orientation, they naturally grow very well aligned making their integration in microelectronic processes much simpler [51]. Also, these wires don't have the typical twin facets and stacking faults which implies that they are better suited for high performance devices.

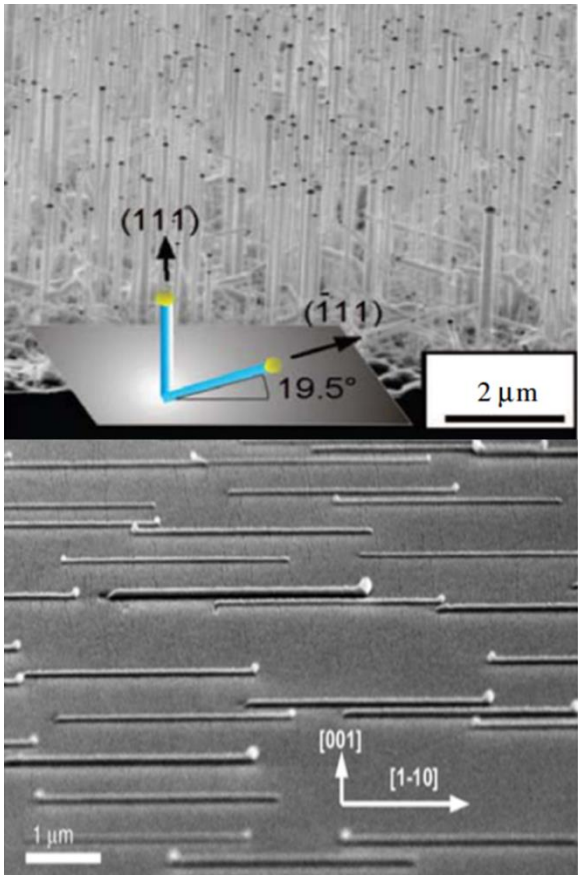

Figure 4.3: SEM images of MOCVD grown GaAs Nanowires grown from surfaces with different surface crystal orientations, (111) (top) and (001) (bottom). Notice that they can be grown laterally and well aligned on the (001) GaAs surface [51].

The use of MOCVD to grow lateral nanowires offers an intriguing opportunity for doping. It is hypothesized that the incorporation of dopants such as silicon, carbon, or zinc may be possible by simply flowing them in vapor phase during growth [52]. Just as the GaAs is adsorbed into the liquid metal alloy catalyst, the dopants may also be adsorbed; once saturation is reached it will be precipitated out as dopants in the GaAs crystalline lattice. In situ doping is a much preferred method of doping because it allows one to make lateral atomically thin PN

interfaces without an additional processing step implying better device performance and simpler processing. In-situ zinc doping was shown to be achievable by flowing the dopant gases in the CVD chamber during growth, however, the details of the doping mechanism was poorly characterized and not well understood [52]. In addition, the unexpected formation of periodic twinned facets formed in the regions of doping implies that more characterization is needed to understand the doping dynamics of in-situ MOCVD doping.

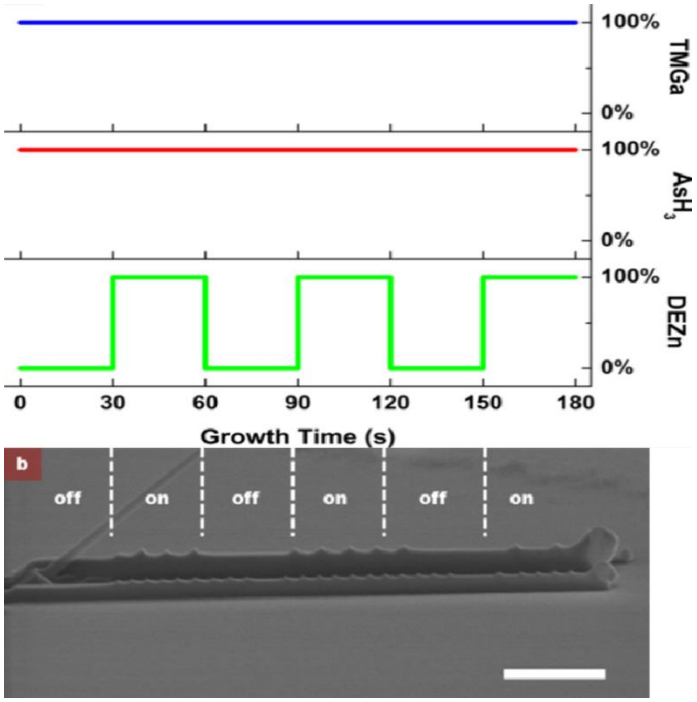

Figure 4.4: (a) Shows the periodic introduction of doping gases labeled as DEZn. (b) SEM image of Nanowire after growth. These figures are aligned in order to show how the introduction of doping gas affects the NW morphology [52].

TEM and SEM analysis confirmed the formation of faceting as a result of a change in morphology in the doping regions. The diffraction contrast TEM image, shown in figure 4.5b,

shows the formation of twinned boundaries with a different morphology leading to contrast (red arrows) within the nanowire. The spatially distribution of dopants and charge in the doping regions was not known, and there was a lack of techniques that had the resolution and sensitivity to identify how the morphology changes affects the electronic properties of the GaAs NW. Microwave Impedance Microscopy has shown the ability to reveal interesting doping and electronics property variations in the laterally grown GaAs Nanowires with ~25nm resolution. It has shown promise in providing the information needed to understand the doping dynamics of in situ doping.

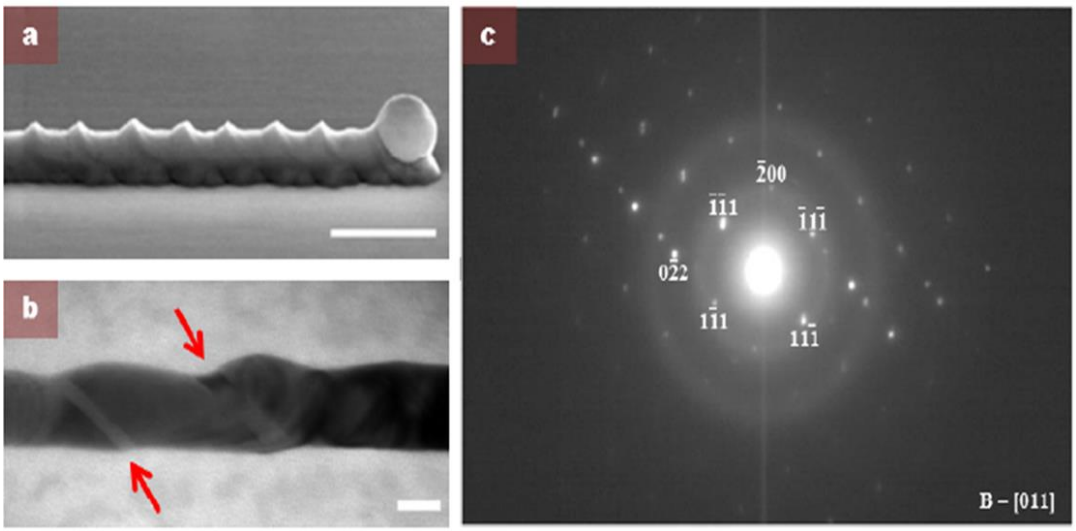

Figure 4.5: (a) high resolution SEM image of the p-doped portion of a GaAs NW showing the periodicity of the twin facets. (b) Ultra high resolution diffraction-contrast TEM image of the corrugations seen in the doped regions revealing local differences in crystalline structure. (c) Diffraction patterns of the GaAs NW shows the presence of two different crystalline orientations present in the faceted regions [52].

4.3 Charge Density Profile Analysis using Microwave Impedance Microscopy

MIM-AFM analysis was performed on as grown GaAs NWs in ambient conditions. The scans obtained were all qualitative and had a maximum resolution of ~25nm. One advantage of using MIM-AFM to characterize NW structures is the ability to directly correlate the capacitance and resistance data to a 3-D topography image in order to see how the morphology influences charge density. In figure 4.6, a wire with only three well-spaced notches is imaged and compared to the calibration sample. Notice that the facets are easily resolved in the 3-D overlay image, and the notches show a distinct capacitance signal which corresponds to a depletion of charge. Although the MIM doesn't provide chemical information regarding the doping distribution on the NWs, it does provide insight to the inhomogeneity of the charge distribution implying that the doping profile is also non-uniform.

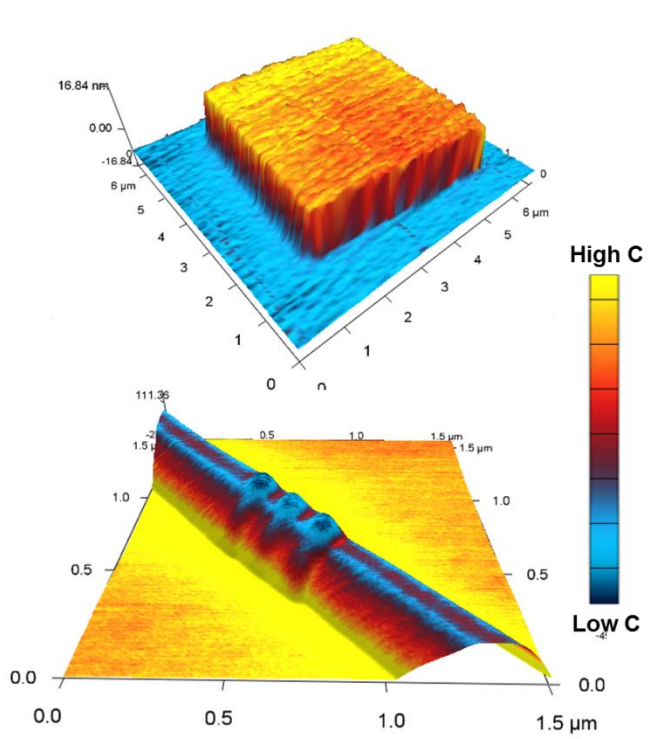

Figure 4.6: MIM Capacitance is overlayed on a 3-D AFM topology map showing how differences in capacitance correlate to surface morphology. The Alumina dot on SiO_2-Si calibration sample (top), shown here as a point of comparison for the MIM image of GaAs NW (bottom).

To further investigate the charge distribution across doped region of the NW structures, wide area, high resolution 3-D resistance and capacitance images were taken on NWs with multiple conjugations. Notice that the resistance and capacitance images are in good agreement, in that areas with the highest charge density, seen in the capacitance channel, tend to have a lower resistance; this is easily seen on the gold catalyst particle near the top of the wire. There are some notable similarities and difference between capacitance and resistive images. Notice that there is charge depletion on all the NW facets including the lateral facet along the length of

the wire and the twinned facets on the notch regions. This charge depletion seem to increase along the growth direction of the NW implying that it is likely directly correlated to the amount of local dopants which also increase along the growth direction. However, this observation is not readily apparent in the resistance images implying that the charge mobility is fairly uniform across the NW length; this is a reasonable observation since the charge mobility across the NW shouldn't differ much from that of pure GaAs since it is the dominate species. However, there are pockets of very low resistance along the length of the wire which prefer to aggregate on the corners of the twinned facets. These pockets are unusual in that they have a low resistance despite being depleted of charge, as seen in the capacitance channel; this indicates that it may be precipitates of the doping species, Zn, but we have been unable to confirm this. In addition, there is an accumulation of charge at the NW-substrate interface implying that there may be a junction that can be seen in both channels, the cause of this phenomenon is unclear.

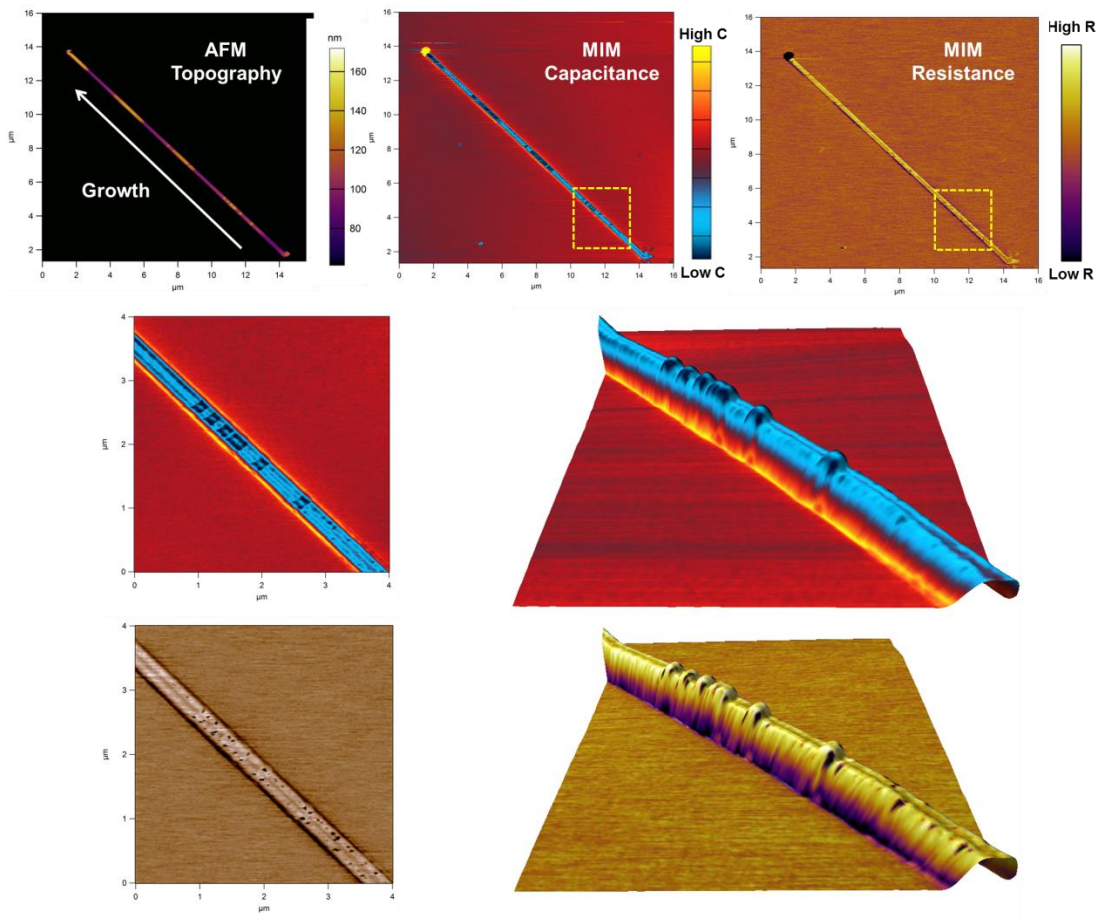

Figure 4.7: At the top are AFM, MIM-C, and MIM-R images of an intermittently doped Nanowire. The bottom images (bottom-left) are higher resolution images of the area highlighted by the yellow box in the top images. 3D overlays (bottom-right) of MIM-C and MIM-R on AFM topology are shown to correlate electrical property data to morphology.

To better analyze the distribution of charge in a notched area we took several lines cuts of a corrugated region to create a topology correlated charge distribution plot in the NW axial direction. We found a repeated trend where there is a small increase in charge at the center of the notch near its geometric peak. It is worth mentioning that there is an increase in charge, greater

than that of the undoped section of the nanowire, in between each notch. It is apparent that each notch has approximately the same capacitance distribution and magnitude implying that the formation of the notches must come from a periodic cyclical doping mechanism when the in-situ dopants are introduced. The ability to take line cuts of the MIM signal and correlate it with the topography is very beneficial to understanding the in-situ doping dynamics of VLS NW growth.

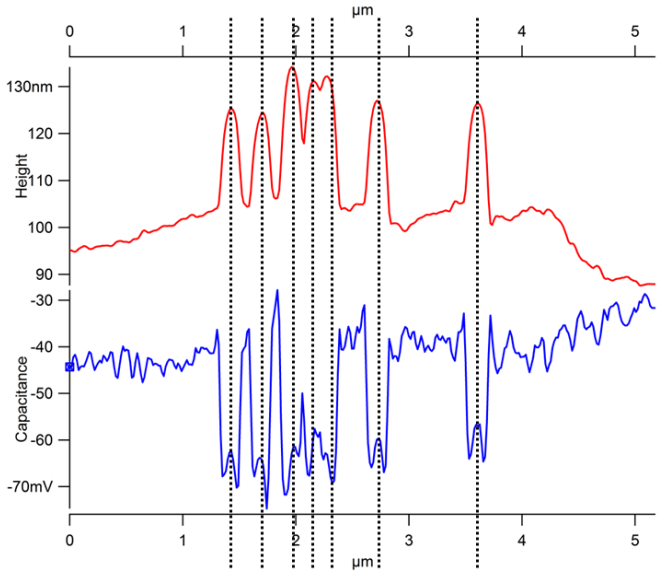

Figure 4.8: Graph showing line cuts of the AFM topology data (top) and MIM Capacitance data. The dotted line is placed at points where there is a local maximum inside the areas of low capacitance; interestingly it correlates exactly to the location of the topographical peaks of the doped notches.

The MIM characterization of laterally grown GaAs Nanowires was very successful at determining the distribution of doping across the nanowire. It is evident that the dopant incorporation into the lattice structure is anisotropic in nature and is strongly correlated to structural features. It appears as though all the faceted regions of the nanowire are depleted of

charge compared to the rest of the nanowire. It is hypothesized that this is due to a high concentration of Zn dopants in the center of the periodic notched regions caused by a cyclical accumulation – supersaturation – purging effect of Zn in the metal catalyst during growth. The Zn incorporated in the GaAs lattice causes the faceting effect and the difference in fermi energy between the notch and the surrounding wire causes charge diffusion which is responsible for the regions of charge depletion. Likewise it is believed that charge diffusion between the nanowire and the substrate is responsible for the charge accumulation (high capacitance) area at the base of the nanowire. It is worth noting that capacitance can be influenced by many different effects simultaneously including dangling bonds and surface states at the facets, and is therefore limited to an indirect measurement of dopant distribution. However, the potential of MIM for exploring the inhomogeneity of electrical properties in novel semiconducting nanowire morphologies is very evident.

CHAPTER 5

NEAR FIELD INFRARED SPECTROSCOPY/MICROSCOPY CHARACTERIZATION OF DOPING DISTRIBUTION IN GAAS NANOWIRES

5.1 Introduction to Tip Enhanced Optical Spectroscopy/Microscopy

Optical Spectroscopy is a common way to identify differences in material's composition by studying differences in optical behavior. This can result from chemical and structural differences revealed by the material's energy spectrum. Infrared Laser Absorption spectroscopy can probe the number of active IR phonon states available at a particular IR wavelength determined by the frequency dependent dielectric response; this response is a result of the material's distinct IR energy spectra [53]. There have been many successes in using different forms of spectroscopy to determine differences in nanoscale properties [54]. However, spectroscopy characterization of nanostructures have a characteristic shortcoming in that it is difficult to get the sub-diffraction resolution needed to see detailed structurally driven phenomena. The most recent developments in AFM have been combining the AFM with spectroscopy techniques. The idea is to couple the incident laser light to a very sharp AFM tip, this creates a near-field effect which confines the strongest optical response just below the tip apex. Then the spectroscopic data collected by a photodiode can be spatially correlated to the position of the AFM tip which vastly improves the spatial resolution of the spectroscopy technique beyond the diffract limit.

For Near Field IR Microscopy the signal enhancement of the incident IR laser source is due to the near-field effects from the tip sharpness and is much less sensitive to the tip's

geometry since the incident wavelength, >1um for mid-infrared, is typically much larger than the tip dimensions near the apex making the near-field coupling non-resonant in nature [55]. As a result, the NFIR incident E-field strength is frequency independent, hence the tip's overall sharpness is more important than the constantly changing tip geometry making the data obtained more reliable and reproducible than other near-field spectroscopy techniques such as Tip Enhanced Raman Spectroscopy.

The use of NFIR spectroscopy has been used to map doped semiconductor nanowires [56]. The dopant profile of VLS vertically grown InP NWs was preformed showing the resourcefulness of this technique for mapping the doping domains in III-V nanowires [57]. The NW showed distinct contrast in the amplitude and phase between the regions doped with Sulfur region in-between two undoped regions as seen in figure 5.1.

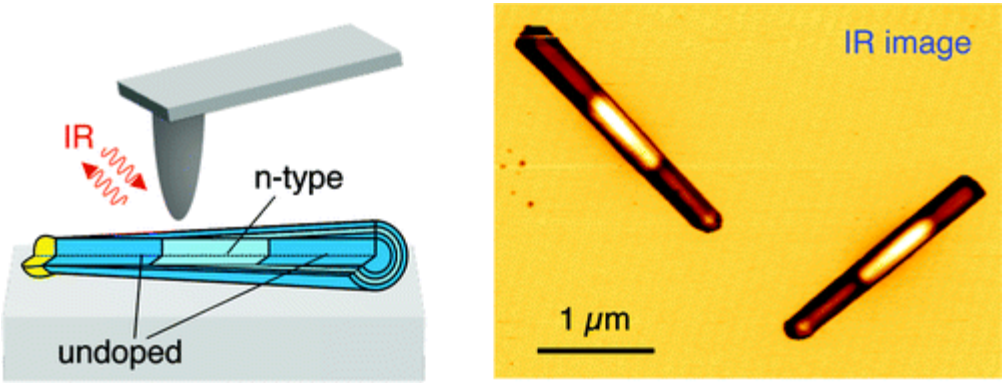

Figure 5.1: Simple schematic showing the NFIR measurement technique on doped InP nanowires (left). High resolution NFIR image of doped InP nanowire clearly showing doping contrast [58].

5.2 Theory of Near-Field Infrared Spectroscopy and Instrumentation

For our purposes the NFIR the observable is the backscattered signal at a fixed frequency set to the mid-IR resonant frequency of the plasmonic free-carrier oscillations [58,59]. The backscatter signal is a nonlinear response to the sample's dielectric constant at the fixed frequency which is linearly correlated to the local charge density of the sample according to the following equation called the Drude Model [59]:

$$\varepsilon(\omega_{IR}) = \varepsilon_{\infty}\left(1 - \frac{{\omega_{plasma}}^2}{{\omega_{IR}}^2 + i\omega_{IR}\gamma}\right) \sim \frac{n}{{\omega_{IR}}^2 + i\frac{\omega_{IR}}{\mu}}$$

Where n is the free-carrier concentration and μ is the free carrier mobility. This equation only applies for Metals and highly doped semiconductors; for lesser doped semiconductors the presence of optical phonon assisted absorption will affect the dielectric constant which is the case for our experiment. However it does imply that changes in carrier density which is correlated to the doping distribution will result in contrast. It is worth noting that the in the case of charge accumulation and depletion regions, which naturally occurs from charge carrier diffusion, the charge density distribution detected using NFIR does not give information regarding the spatial distribution of dopants.

The backscatter signal have two components: the background (far-field) backscatter and the near-field back scatter. The magnitude the near-field falls off rapidly as distance from the tip apex increases and has a much stronger dependence on tip-sample distance, modulated by the tapping mode frequency of the AFM cantilever, than the background backscatter [59]. To

separate the two forms of the signal the mirror, as seen in figure 5.2, is used to change the phase of the incident laser in order modulate the overall incident signal strength. Subsequently, the observed modulated backscatter signal has sub-bands in the frequency domain which correspond to $f_{backscatter}(n,m) = n*f_{cantilever} \pm m*f_{mirror}$, where n and m are integer modes [59]. At higher order n values the magnitude of the background signal falls significantly more than the near-field signal, thus the magnitude of the signal from the mirror modulation should be dominated by the near-field response for n>1. It can be derived that optical amplitude and phase signal use to create the images throughout this chapter are a function of the demodulated signal at $f_{backscatter}(2,1)$ and $f_{backscatter}(2,2)$ [60].

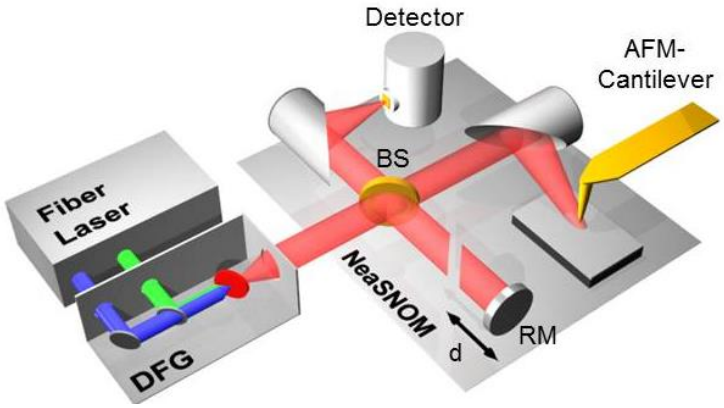

Figure 5.2: This shows a simple schematic of the NFIR system used in this research [61].

Simulations show that both the optical amplitude and phase signal relies non-linearly on doping density [59]. Unlike the MIM-C observable which can be qualitatively interpreted as local sample capacitance, for NFIR the magnitude of the signal cannot be directly interpreted as relative charge density without a detailed quantitative analysis. For this study, this technique is an ideal complement to MIM because it can produce high resolution, ~10nm, spatial contrast

profiles based on large variations in the local free carrier density, in this case from spatially confined domains of Zn doping.

5.3 Doping Profile Observation using Near-Field Infrared Microscopy on GaAs Nanowires

In Figure 5.3, a very high resolution, small scan (~4um) linecut was taken with NFIR, MIM, and AFM along the doping region on same GaAs NW for a direct comparison. For the image comparison the three conjugated sections are readily apparent; although the NFIR uses a smaller tip (~10nm) implying a higher resolution, MIM image clearly has a higher signal sensitivity and signal to noise level producing a more detailed image. When comparing the signal response to MIM under the calibrated conditions stated above the NFIR optical amplitude signal, which was inverted in figure 5.3 for easier comparison, shows the same exact trend. This observation solidifies the idea that the presence of dopants, seen in the NFIR data, leads to a depletion of free carriers, seen in the MIM data, likely induced by a local space charge region near the ionized Zn dopants.

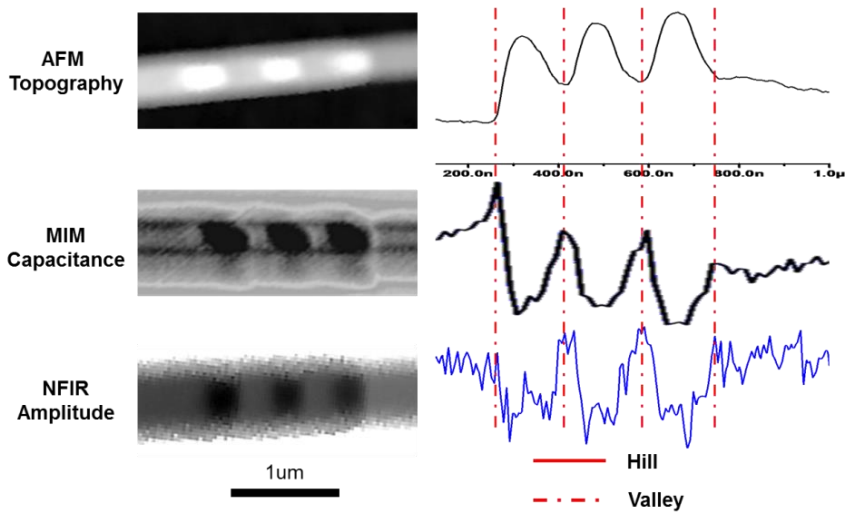

Figure 5.3: These are images (left) and linecuts (right) of the same doped nanowire region taken by AFM, MIM, and NFIR which are spatially aligned for easy comparison. The NFIR amplitude image and linecut were flipped to more easily show the similarity in the trends between the two techniques. The dotted line show the location of the topographical valley in between the notches.

High resolution NFIR images were also taken of the GaAs NWs with multiple spaced out conjugations. In these images both the optical amplitude and phase varied with doping profile. By acquiring the scans with a wider area and taking several line averages we were able to increase the smoothness and overall contrast of the image despite losing resolution. Linecuts of the optical phase reveals a familiar doping characteristic of the more spaced out correlations, where there is a small decrease in the amount of zinc dopants in the center of the notch, which reaffirms that dopants are unevenly distributed in a single notch and is in good agreement with MIM observations.

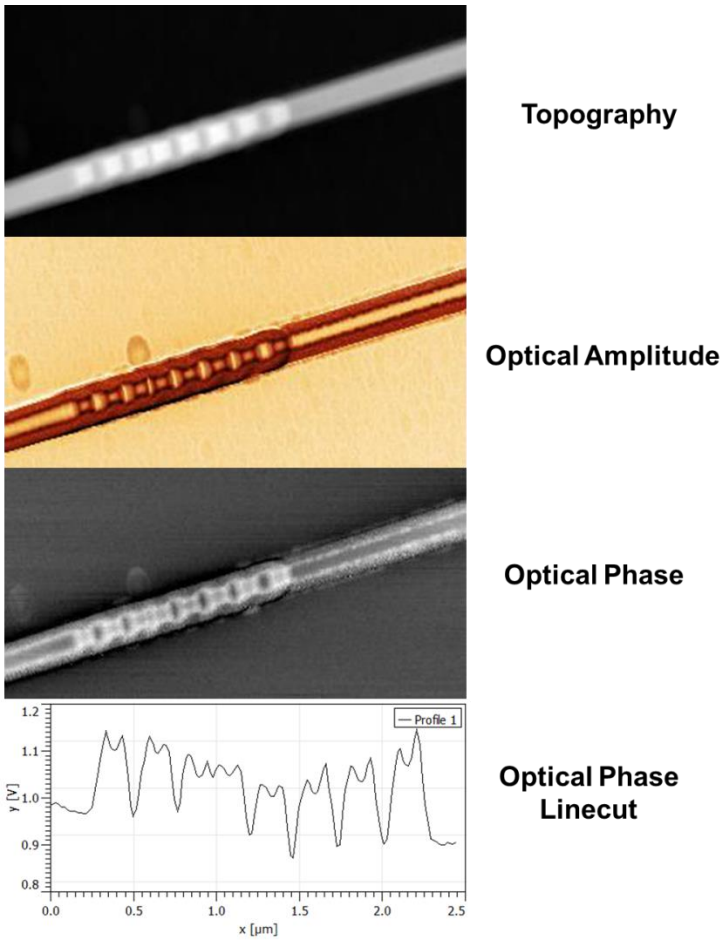

Figure 5.4: Images of topography, optical amplitude, and optical phase obtained simultaneously in a single NFIR scan of a nanowire.

The single to noise of the NFIR analysis of GaAs NW was improved when imaging a higher doped sample under slow scanning conditions with a fresh tip. Also, one should tune the incident laser wavelength to find the best operating point for maximum contrast between the on and off resonant species. Finding the ideal wavelength is not intuitive because the resonant plasmon frequency may be subtly different for different doping conditions. We were able to resolve the doping profile on multiple closely spaced corrugations with superb resolution as seen

in figure 5.5. Notice that the dopants (dark) tend to accumulate near edges of the notch and on the nanowire-substrate interface similar to the observations made in MIM and figure 5.5. A shadow artifact is apparent on one side of the nanowire from the angle difference between the incident laser and photodetector.

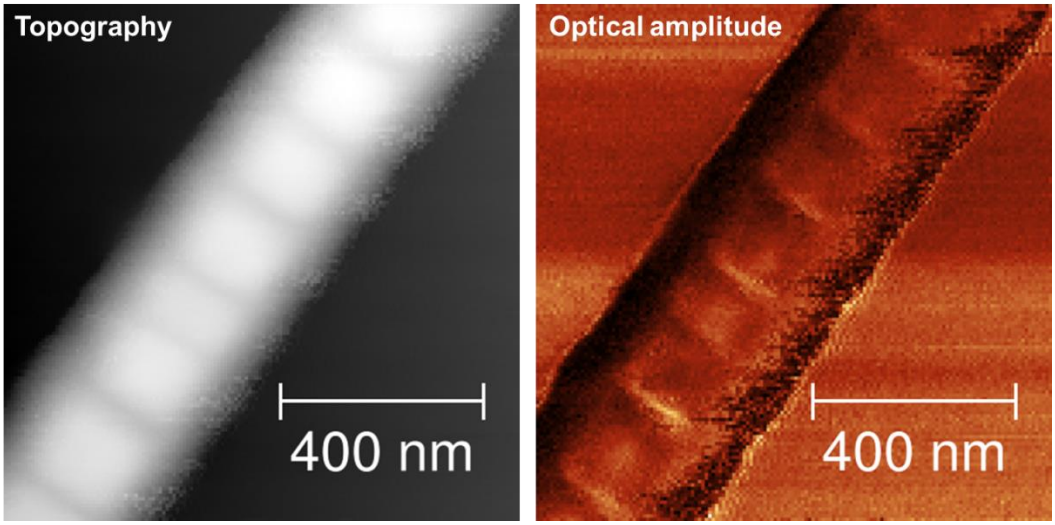

Figure 5.5: Super high resolution NFIR topography and optical amplitude image of the Zn doped portion of a nanowire.

NFIR is a great compliment to doping characterization using MIM. Many of the trends and patterns in the signal match perfectly with that of MIM. For highly doped semiconductors both the NFIR absorption spectra and MIM capacitance are directly related to the charge density, however they are generally not directly correlated. Thus, in order to realize this experimentally a well characterized calibration sample may to be used to better correlate the MIM to NFIR signal contrast. In addition, to improve the SNR much more NFIR data has to be collected in order to find the ideal incident wavelength for maximum signal response. The use of both techniques

offers an intriguing opportunity to see nanoscale phenomena on the individual Nanowire scale. This may help the optimization of VLS growth and in-situ doping in order to improve the reproducibility of NW electronic characteristics.

REFERENCES

1 Ziegler, D., & Stemmer, A.. Force gradient sensitive detection in lift-mode Kelvin probe force microscopy. *Nanotechnology,* (2011) 075501-075501.

2 Avila, A., & Bhushan, B. Electrical Measurement Techniques in Atomic Force Microscopy. *Critical Reviews in Solid State and Materials Sciences,* (2010) 38-51.

3 Kikukawa, Atsushi, Sumio Hosaka, and Ryo Imura. "Silicon pn junction imaging and characterizations using sensitivity enhanced Kelvin probe force microscopy." *Applied Physics Letters* 66.25 (1995): 3510-3512.

4 Bhushan, Bharat, and Anton V. Goldade. "Measurements and analysis of surface potential change during wear of single-crystal silicon (100) at ultralow loads using Kelvin probe microscopy." *Applied surface science* 157.4 (2000): 373-381.

5 Müller, F., et al. "Applications of scanning electrical force microscopy."*Microelectronics Reliability* 37.10 (1997): 1631-1634.

6 Jacobs, H. O., H. F. Knapp, and A. R. O. S. I. Stemmer. "Practical aspects of Kelvin probe force microscopy." *Review of Scientific Instruments* 70.3 (1999): 1756-1760.

7 Sugimura, Hiroyuki, et al. "Potential shielding by the surface water layer in Kelvin probe force microscopy." *Applied physics letters* 80.8 (2002): 1459-1461.

8 Garcia-Martin, Antonio, and Ricardo Garcia. "Formation of nanoscale liquid menisci in electric fields." *Applied physics letters* 88.12 (2006): 123115.

9 Ito, Masanao, et al. "Local potential profiling of operating carbon nanotube transistor using frequency-modulation high-frequency electrostatic force microscopy." *Applied Physics Letters* 102.1 (2013): 013115.

10 Bae, S. S., et al. "Characterizing defects and transport in Si nanowire devices using Kelvin probe force microscopy." *Nanotechnology* 23.40 (2012): 405706.

11 E.J. Fuller, D. Pan, B.L. Corso, O.T. Gül & P.G. Collins. Mean free path in single-walled carbon nanotube measured by Kelvin Probe microscopy. *Phys. Rev. B* 89, 245450 (2014).

12 Palermo, Vincenzo. et al. Exploring nanoscale electrical and electronic properties of organic and polymeric functional materials by atomic force based approaches. *Chem. Commun.,* 3326-3337. DOI: 10.1039/B701015J (2007)

13 Williams, C. C. "Two-dimensional dopant profiling by scanning capacitance microscopy." *Annual review of materials science* 29.1 (1999): 471-504.

14 Lai, K., Kundhikanjana, W., Kelly, M. & Shen, Z. X. Modeling and characterization of a cantilever-based near-field scanning microwave impedance microscope. *Review of Scientific Instruments* 79, doi:Artn 063703 Doi 10.1063/1.2949109 (2008).

15 Lai, K., Ji, M. B., Leindecker, N., Kelly, M. A. & Shen, Z. X. Atomic-force-microscope-compatible near-field scanning microwave microscope with separated excitation and sensing probes. Review of Scientific Instruments 78, doi:Artn 063702 Doi 10.1063/1.2746768 (2007).

16 Tselev, A., Anlage, S. M., Ma, Z. K. & Melngailis, J. Broadband dielectric microwave microscopy on micron length scales. Review of Scientific Instruments 78, doi:Artn 044701 Doi 10.1063/1.2719613 (2007).

17 Yang, Y. et al. Batch-fabricated cantilever probes with electrical shielding for nanoscale dielectric and conductivity imaging. J Micromech Microeng 22, doi:10.1088/0960-1317/22/11/115040 (2012).

18 Lai, K., Kundhikanjana, W., Kelly, M. A. & Shen, Z. X. Calibration of shielded microwave probes using bulk dielectrics. Applied Physics Letters 93, doi:Artn 123105 Doi 10.1063/1.2990638 (2008).
19 Smoliner, J., et al. "Scanning microwave microscopy/spectroscopy on metal-oxide-semiconductor systems." *Journal of Applied Physics* 108.6 (2010): 064315.
20Avouris, P. Carbon nanotube electronics and optoelectronics. *Mrs Bull* 29, 403-410, doi:Doi 10.1557/Mrs2004.123 (2004).
21 Avouris, P., Martel, R., Derycke, V. & Appenzeller, J. Carbon nanotube transistors and logic circuits. *Physica B* 323, 6-14, doi:Pii S0921-4526(02)00870-0 Doi 10.1016/S0921-4526(02)00870-0 (2002).
22 Kocabas, C. *et al.* Guided growth of large-scale, horizontally aligned arrays of single-walled carbon nanotubes and their use in thin-film transistors. *Small* 1, 1110-1116, doi:DOI 10.1002/smll.200500120 (2005).
23 Kocabas, C. *et al.* Radio frequency analog electronics based on carbon nanotube transistors. *Proceedings of the National Academy of Sciences of the United States of America* 105, 1405-1409, doi:DOI 10.1073/pnas.0709734105 (2008).
24 Lan, Y., Wang, Y. & Ren, Z. F. Physics and applications of aligned carbon nanotubes. *Advances in Physics* 60, 553 678, doi:10.1080/00018732.2011.599963 (2011).
25 Cao, Q., Han, S. J., Tulevski, G. S., Franklin, A. D. & Haensch, W. Evaluation of Field-Effect Mobility and Contact Resistance of Transistors That Use Solution-Processed Single-Walled Carbon Nanotubes. *Acs Nano* 6, 6471-6477, doi:Doi 10.1021/Nn302185d (2012).
26 Cao, Q. & Han, S. J. Single-walled carbon nanotubes for high-performance electronics. *Nanoscale* 5, 8852-8863, doi:Doi 10.1039/C3nr02966b (2013).
27 He, M. *et al.* Chiral-Selective Growth of Single-Walled Carbon Nanotubes on Lattice-Mismatched Epitaxial Cobalt Nanoparticles. *Sci Rep-Uk* 3, doi:10.1038/srep01460 (2013).
28 Rutherglen, Chris, Dheeraj Jain, and Peter Burke. "Nanotube electronics for radiofrequency applications." *Nature Nanotechnology* 4.12 (2009): 811-819.
29 Ilani, S., Donev, L. A. K., Kindermann, M. & McEuen, P. L. Measurement of the quantum capacitance of interacting electrons in carbon nanotubes. Nature Physics 2, 687-691, doi:Doi 10.1038/Nphys412 (2006).
30 Bulashevich, K. A. & Rotkin, S. V. Nanotube devices: A microscopic model. Jetp Lett+ 75, 205-209, doi:Doi 10.1134/1.1475724 (2002).
31 Luryi, S. Quantum Capacitance Devices. Applied Physics Letters 52, 501-503, doi:Doi 10.1063/1.99649 (1988).
32 The experimental conditions for this work used a typical tip radius of ~50nm with a dielectric overlayer thickness of 3.5nm.
33 Tselev, A. *et al.* Near-field microwave microscope with improved sensitivity and spatial resolution. *Review of Scientific Instruments* 74, 3167-3170, doi:Doi 10.1063/1.1571954 (2003).
34 Lai, K., Kundhikanjana, W., Kelly, M. & Shen, Z. X. Modeling and characterization of a cantilever-based near-field scanning microwave impedance microscope. *Review of Scientific Instruments* 79, doi:Artn 063703 Doi 10.1063/1.2949109 (2008).
35 Lai, K. *et al.* Nanoscale Electronic Inhomogeneity in In2Se3 Nanoribbons Revealed by Microwave Impedance Microscopy. *Nano letters* 9, 1265-1269, doi:10.1021/nl900222j (2009).

36 Drycke, V., Martel, R., Appenzeller, J. & Avouris, P. Controlling doping and carrier injection in carbon nanotube transistors. *Applied Physics Letters* 80, 2773-2775, doi:Doi 10.1063/1.1467702 (2002).
37 Rochefort, A. & Avouris, P. Electron interference effects on the conductance of doped carbon nanotubes. *Journal of Physical Chemistry A* 104, 9807-9811, doi:Doi 10.1021/Jp002690z (2000).
38 Duan, Xiangfeng, et al. "High-performance thin-film transistors using semiconductor nanowires and nanoribbons." *Nature* 425.6955 (2003): 274-278.
39 Blekker, Kai, et al. "High-frequency measurements on InAs nanowire field-effect transistors using coplanar waveguide contacts." *Nanotechnology, IEEE Transactions on* 9.4 (2010): 432-437.
40 Liu, Xi, et al. "Large-scale integration of semiconductor nanowires for high-performance flexible electronics." *Acs Nano* 6.3 (2012): 1888-1900.
41 Persson, K-M., et al. "Extrinsic and intrinsic performance of vertical InAs nanowire MOSFETs on Si substrates." (2013): 1-1.
42 Long, Yun-Ze, et al. "Recent advances in large-scale assembly of semiconducting inorganic nanowires and nanofibers for electronics, sensors and photovoltaics." *Chemical Society Reviews* 41.12 (2012): 4560-4580.
43 Fortuna, Seth A., and Xiuling Li. "GaAs MESFET with a high-mobility self-assembled planar nanowire channel." *Electron Device Letters, IEEE* 30.6 (2009): 593-595.
44 Pillarisetty, Ravi. "Academic and industry research progress in germanium nanodevices." *Nature* 479.7373 (2011): 324-328.
45 Buin, A. K., et al. "Significant enhancement of hole mobility in [110] silicon nanowires compared to electrons and bulk silicon." *Nano letters* 8.2 (2008): 760-765.
46 Riel, Heike, et al. "III–V compound semiconductor transistors—from planar to nanowire structures." *MRS Bulletin* 39.08 (2014): 668-677.
47 G. Signorello, S. Karg, E. Lörtscher, P. A. Khomyakov, B. Gotsmann, M. Björk, D. L. Dheeraj, H. Weman, H. Riel, "Uniaxial Stress in GaAs Nanowires Reveals an Unprecedented Light Emission Tunability and Novel Bandstructure Transitions," *Communications of the Swiss Physical Society* 45, 29. (2014)
48 H. Fahad, M. M. Hussain. "Are Nanotube Architectures More Advantageous Than Nanowire Architectures For Field Effect Transistors?". Scientific Reports 2, Article number: 475 doi:10.1038/srep00475 (2012)
49 S.A. Fortuna, J. Wen, I.S. Chun, and X. Li, "Planar GaAs Nanowires on GaAs (100) Substrates: Self-Aligned, Nearly Twin-Defect Free, and Transfer-Printable", Nano Letters (2008).
50 R. S. Dowdy, D. A. Walko, and X. Li, "Relationship between plannar GaAs nanowire growth direction and substrate orientation" Nanotechnology 24, 035304 (2013).
51 S.A. Fortuna and X. Li, "Metal-catalyzed semiconductor nanowires: a review on the control of growth directions", Semicond. Sci. Technol. 25 (2010) 024005.
52 R. Dowdy, C. Zhang, P. K. Mohseni, S. A. Fortuna, J-G Wen, J. J. Coleman, and X. Li, "Perturbation of Au-assisted Planar GaAs Nanowire Growth by p-Type Dopant Impurities", Optical Materials Express Vol. 3, Issue 10, pp. 1687-1697 (2013).
53 Kuhlmann, U., et al. "Infrared active phonons in single-walled carbon nanotubes." *Chemical Physics Letters* 294.1 (1998): 237-240.

54 Dresselhaus, M. S., et al. "Single nanotube Raman spectroscopy." *Accounts of Chemical Research* 35.12 (2002): 1070-1078.

55 Bründermann, Erik, and Martina Havenith. "SNIM: Scanning near-field infrared microscopy." *Annual Reports Section" C"(Physical Chemistry)* 104 (2008): 235-255.

56 Huber, Andreas J., et al. "Simultaneous IR Material Recognition and Conductivity Mapping by Nanoscale Near-Field Microscopy." Advanced Materials 19.17 (2007): 2209-2212.

57 Stiegler, J. M., et al. "Nanoscale free-carrier profiling of individual semiconductor nanowires by infrared near-field nanoscopy." *Nano letters* 10.4 (2010): 1387-1392.

58 Stiegler, J. M., et al. "Correlative infrared–electron nanoscopy reveals the local structure–conductivity relationship in zinc oxide nanowires." *Nature communications* 3 (2012): 1131.

59 Stiegler, J. M. "Infrared Spectroscopic Near-Field Microscopy of Nanoparticles and semiconducting nanowires. PhD thesis at the University of Pais Vasco (2012)

60 N. Ocelic, A. Huber, and R. Hillenbrand. Pseudoheterodyne detection for background-free near-field spectroscopt. Applied Physics Letters, 89(10): 101124 (2006)

61 F. Huth, A. Govyadinov, S. Amarie, W. Nuansing, F. Keilmann, R. Hillenbrand, "Nano-FTIR-Nanoscale chemical mapping by local infrared fingerprint". Nanoletters 12, (2012): 3973

APPENDIX A: MIM-AFM IMAGING PROCEDURES

General Procedures:

1. Load the MIM tip into the tip holder and secure into the AFM
2. Preform MIM calibration on calibration sample
3. Use AC mode to find target area on the sample
4. Use MIM-AFM scan in contact mode to acquire high resolution image
5. Post process the data (3D overlays look very nice...)

Calibration Notes:

- Disabling slow scan over Al2O3 dots makes calibration easier
- Always record and save the phase offset and Al2O3 dots image to figure out which pathway the C-signal is in and which direction is high Capacitance. **(Note: the capacitance can be in either I or Q signal pathway and high capacitance can be negative or positive changes in voltage.)**
- Note the S/N ratio by taking a line cut of the Al2O3 dots. Signal > ~±20mV is necessary for high quality images… If the S/N is too low than it indicates either that there is an issue with the tip loading or the tip may be too sharp.
- The MIM tip acts as a RF antenna, thus there is an inverse tradeoff between tip sharpness and sensitivity; tips that are too sharp have low S/N and great resolution, whereas tips that are too dull have poor resolution and very high S/N. The tip can be dulled purposely according to the dimensions of the sample and desired sensitivity/contrast of the scan. (Note: tips will dull as the scan progresses according the relative hardness of the sample.)
- During calibration the signal in the resistive channel will never be completely nullified.

Calibration Procedures:

1. Load MIM tip into the AFM
2. Input calibration sample in AFM
3. Preform frequency sweep (set # of points to 81) then auto null. Ensure that the dip is lower -20dB, if not then there is a problem with the MIM tip loading.

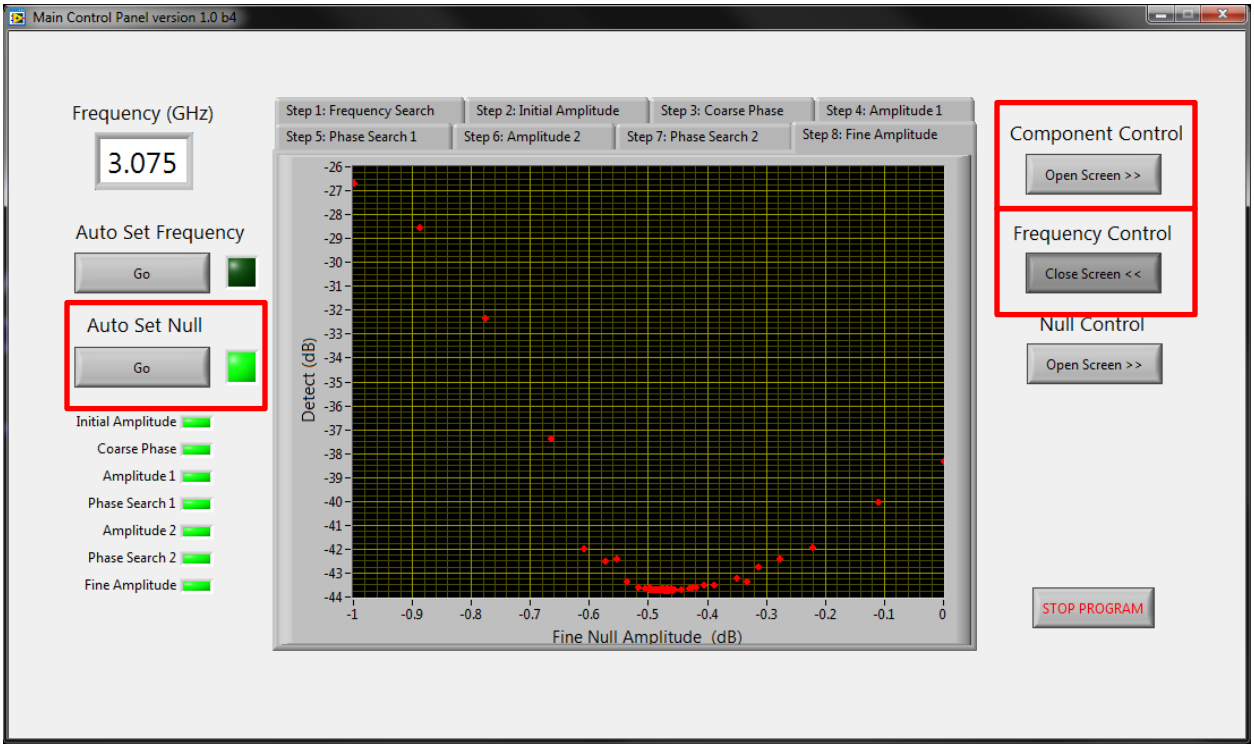

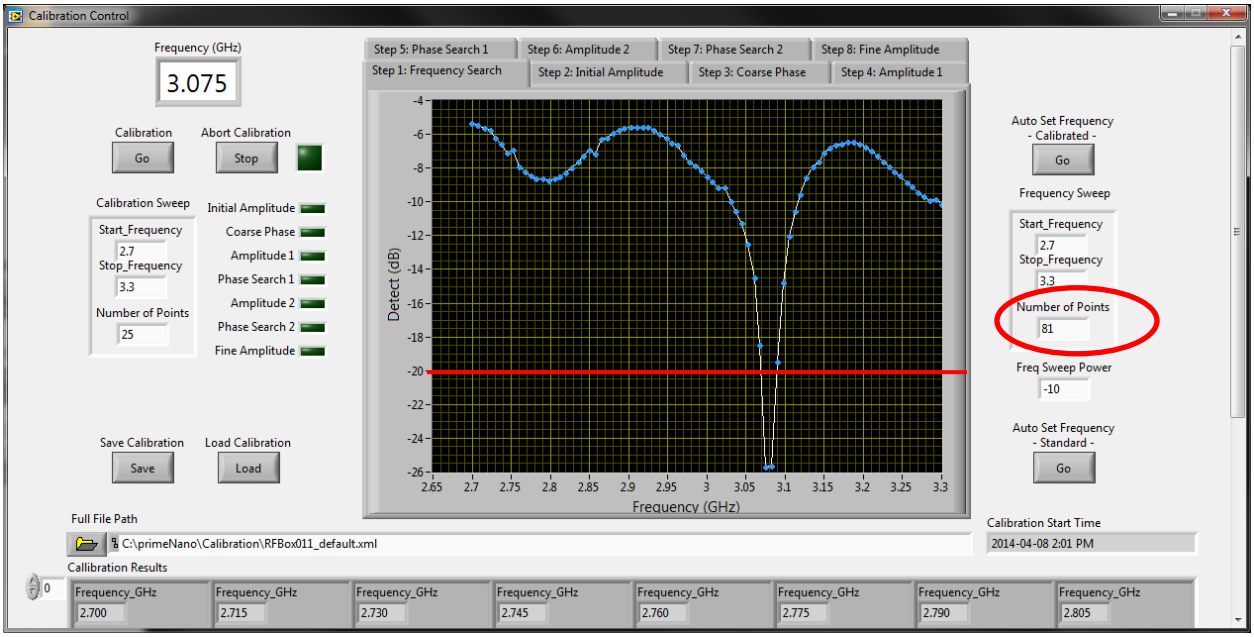

4. Start MFP3D
5. Pick the “Peak” option on the pop-up menu, then close the menu
6. Select the “MIM_contact_mode” experiment file on the desktop (this file has all the general settings for MIM preloaded)
7. Align the Laser on the middle of the tip and zero the deflection
8. Find clean area on the calibration sample and start tip approach

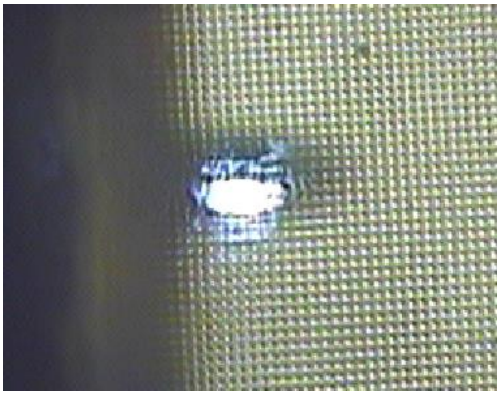

9. Start scan (disabling the slow scan option may help with calibration)
10. Adjust the “demod phase” offset until all the signal is in the capacitance channel in the “component control menu”

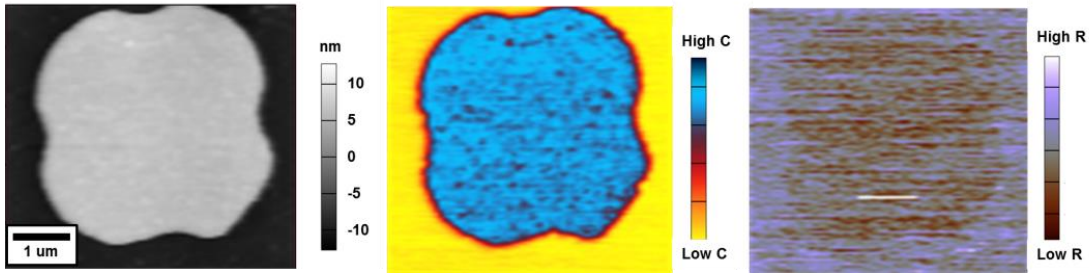

11. Check the S/N level, if it is too low then the tip may be too sharp

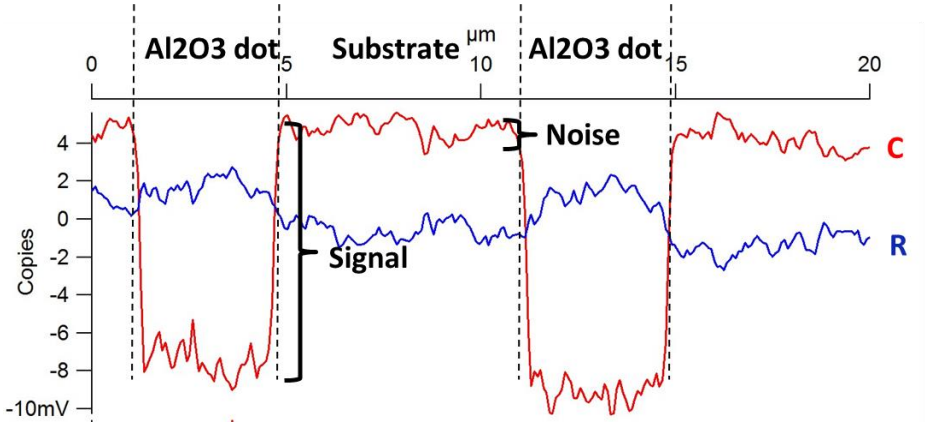

12. If the S/N is too low then disable slow scan over the Al2O3 dots, slowly increase the set point until ~0.5V; as the tip broadens the S/N increases. Once the desired S/N is obtained then withdraw and auto null. Repeat steps 8-11.

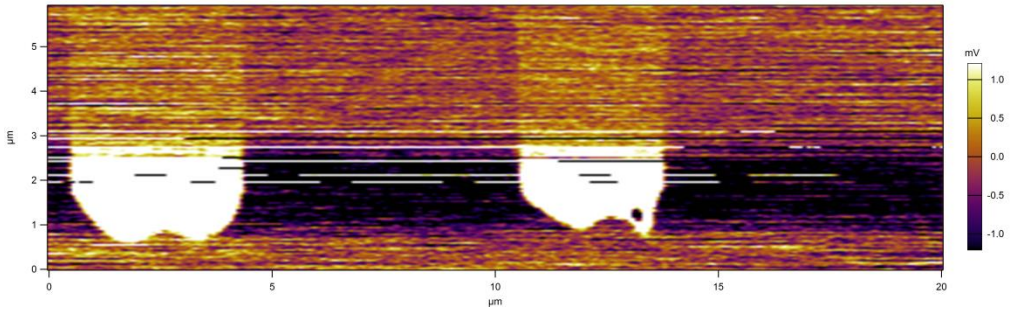

13. Save image

Image Acquisition Notes:

- Scanning at 45degrees can eliminate some tip affects which may improve resolution
- The MIM signal will drift as the scan persists which is why flattening the image is important. If the I or Q voltages drifts >3V, then consider using the "auto null" in-between scans.
- Note that the smallest feature size is ~20nm so adjust the pixel size accordingly
- When picking a new place on the sample after switching to AC mode may have to redo a slow tip approach and auto tune.
- Increasing the "power set" on the component control panel will increase the sample volume which may also improve S/N. It can also cause hysteresis is set too high so avoid going above -3dB if possible

Image Acquisition Procedures:

1. Put the desired sample into the AFM
2. Find the desired area on the sample
3. Switch to AC mode
4. Auto Tune @ 1V, put the set point at 950mV. Typical piezo frequency is between 50-100kHz.

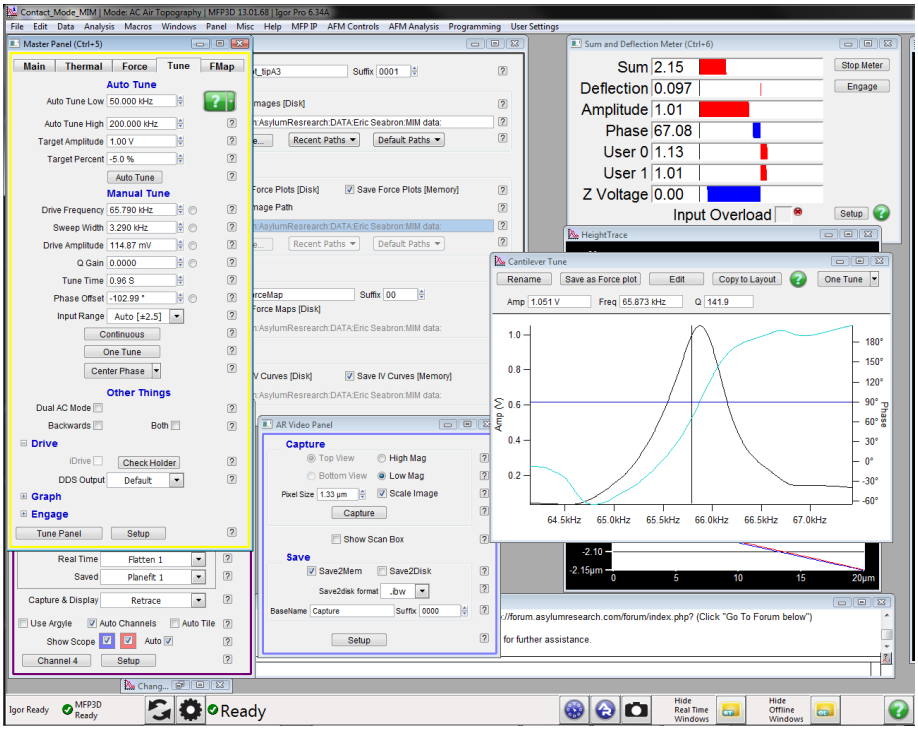

5. Start the slow tip approach (Note: the idea is not to obtain a high quality image, rather to find the ideal part of the sample without damaging the tip)
6. Once the desired area is found, click withdraw tip and switch back to contact mode. Ensure that the set point ~250mV. Engage the sample, auto null, then acquire MIM image.
7. Repeat steps 3-6 in order to image other parts of the sample.